Rosenstiel School of Marine and Atmospheric Sciences
University of Miami

Mechanisms for Transient Seasonal Variability of the Florida Current transport

A MSc Thesis Proposal Submitted by

Ricardo Domingues

MPO / RSMAS

rdomingues@rsmas.miami.edu

to

Chair Dr. William E. Johns, *MPO*

Dr. Mohamed Iskandarani, *MPO*

Dr. Chris Meinen, *NOAA/AOML*

Miami, Florida, USA

December 9, 2015

Contents

List of Figures **ii**

List of Tables **vi**

1 Introduction **1**

2 Scientific Background **3**

2.1 Variability of the Florida Current transport 3

2.2 Westward propagating signals in the North Atlantic 5

2.3 Eddy-related variability at North Atlantic's western boundary 10

2.4 Eddy-wall mechanisms 12

3 Questions **14**

4 Proposed Work **15**

4.1 Regional Ocean Modeling System - ROMS 15

4.2 Numerical experiments 16

4.3 The feature model approach 18

5 Preliminary Results **21**

5.1 Initialization & Open-ocean Processes 21

5.2 Responses at the western boundary 24

5.2.1 Experiment Prel-E01 24

5.2.2 Experiment Prel-E02 27

5.2.3 Experiment Prel-E03 30

6 Summary **31**

References **34**

List of Figures

1 Location of the Florida straits. Highlighted are the locations of the telefone cables used to estimate the Florida Current volume transport, and the location of relevant landmarks in the region of study, such as the Northwest Providence Channel (NWPC). Thin black lines show bathymetric contours every 200 m for depths between 100 m and 1000 m, while thin gray lines show bathymetric contours every 20 m for depths shallower than 100 m. . . 43

2 (a) Florida Current transport time-series (raw, light gray line) derived from measurements of voltage differences accross the straits of Florida using telephone cables. Overlaid is the climatological annual cycle for the Florida Current during 1985-2013 (red line) and the transient component (blue line). (b) Seasonal variability of the Florida Current transport during 1985-2013. (c) Wavelet transform for the Florida Current transport. The thick white lines highlight peaks in the spectral power that are significant at the 95% confidence level, while the black line marks the cone of influence for the analysis. The magenta lines delimits the 73-525 days frequency band. . . 44

3 SHA Root Mean Square along 27°N based on: raw (blue line), annual cycle (red line), high-frequency component ($<$ 73 days, gray line), low-frequency component($>$ 525 days, green line), 73-525 days frequency band (blue line). 45

4 SHA field for March 1st, 2000, filtered at the 73-525 days frequency band. Overlaid is the SHA-derived surface geostrophic velocity vectors. 45

5 (a) SHAr hovmoller (longitude-time) diagram along 27°N. (b) Normalized power spectrum density from SHAs along 27°N for each longitude. (c) Wavelengths associated with SHAr along 27°N estimated using a fast-fourier transform. 46

6 (a) Internal radius of deformation based on climatological conditions the Word Ocean Atlas 2013 calculated using Equations . (b) westward propagating phases speeds for long, linear, first-baroclinic Rossby waves. 47
7 Dispersion relationship for first mode baroclinic rossby waves setting Rd equal to 47 km at 27°N, and using equal zonal and meridional wavenumbers (k=l, blue line), and also setting setting the meridional wavenumber to zero (l=0, red line). 47
8 (a) Model domain used for numerical experiments developed in this study using ROMS. The grid has an horizontal resolution of aproximately $^{1/25}$degree with 540 X 390 points. (b) Grid configurations shown in detail at the Florida Straits. The magenta lines show the location of sections across (c) the Florida Straits, and (d) the Northwest Providence Channel, showing the configuration of vertical layers at these locations. 48
9 (a) Temperture, (b) salinity, and (c) density profiles used as background conditions for model initialization, and its derived (d) buoyancy frequency. Baroclinic modes linked with the (e) vertical velocity and density structure, and with the (f) horizontal velocity and pressure field. Modes are solved using a rigid-lid boundary condition. In panel (e), the modified first baroclinic mode for vertical velocity ($\phi_{1_m}(z)$) is shown as the thick black line. . . 49
10 Gaussian function used to apply vertical displacements on isopycnal surfaces, where D_E is the radius of the eddy, and ΔZ_{max} is the maximum vertical displacement allowed. 50
11 (a) Temperature, (b) salinity, and (c) density structure of an anticyclonic feature used as initial conditions for experiment Prel-E01. 50
12 SSH signature during initialization (left column) and during interaction with the western boundary (right column) for experiments Prel-E01, Prel-E02, and Prel-E03. 51

13 Temporal evolution of domain averaged kinetic energy during model spin-up on diagnostic mode for experiments (a) Prel-E01 and (b) Prel-E02. 52
14 (a) Surface velocity field, (b) surface relative vorticity field, and (c) vertical velocity structure of the eddy after full adjustment during spin up phase on diagnostic mode for experiment Prel-E01. 53
15 Hovmoller (longitude-time) diagrams of SSH along 27°N for experiments (a) Prel-E01, and (b) Prel-E02, and along 29°N for experiment (c) Prel-E03. Black lines indicate westward phase propagation. 54
16 (a) Potential vorticity field for experiment Prel-E01 during model initialization. Red dashed-line indicates the path taken by the anticyclonic eddy during model time integration. (b) Time-latitude hovmoller diagram of potential vorticity field along the path taken by the anticyclonic eddy. 55
17 Surface velocity in the proximity and at the Florida Straits for experiment Prel-E01 at: (a) day 210, (b) day 238, (c) day 266, and (d) day 406. 56
18 Time-series of volume transport anomalies across the Florida Straits (26.8°N) from experiments (a) Prel-E01, and (b) Prel-E02. 57
19 Cross-section velocity at the Florida Straits for experiment: (a) Prel-E01 at 210 days; (c) Prel-E02 at 448 days; and (e) Prel-E03 at day 273. Standard deviation associated with cross-section velocity variability generated at the Florida Straits for experiments (b) Prel-E01, (d) Prel-E02, and (e) Prel-E03. . 58
20 (a) Location of coastal SSH time-series retrieved from modeling outputs. (b) Latitude-time hovmoller diagram of coastal SSH for experiment Prel-E01. (c) Correlation coefficients between coastal SSH and meridional transport at the Florida Straits plotted as a function of correlation lag (abscissa) and latitude (ordinate). The location of the Florida Straits (27°N) is highlighted as black circle at zero lag. Panels (d) and (e) exhibit similar results for experiment Prel-E02, and (f) and (g) for experiment Prel-E03. Contours in SSH hovmollers diagrams and in correlation plots are every 0.2 plot units. 59

21 Same as Figure 20, but for SSH time-series retrieved along the shelf break (a). 60
22 (a) Location where SSH time-series were retrieved at the Bahamas for numerical experiments performed in this study. SSH time-series at the Bahamas for experiments (b) Prel-E01, (d) Prel-E02, and (f) Prel-E03. Lagged correlation analysis between bahamas SSH and meridional transport at the Florida Straits based on modeling outputs from experiments (c) Prel-E01, (e) Prel-E02, and (g) Prel-E03. 61
23 Surface velocity in the proximity and at the Florida Straits for experiment Prel-E02 at: (a) day 147, (b) day 259, (c) day 343, and (d) day 448. 62
24 (a) Cross-section velocity at the Northwest Providence Channel for experiment Prel-E02 at 441 days. (b) Standard deviation associated with velocity variability at the Northwest Providence Channel. 63
25 (a) Location of meridional sections (red lines) at the Northwest Providence Channel, where the evolution of zonal cross-section transport for experiment Prel-E02 is evaluated and ploted in (b). Panels (c) and (d) are same as (a) and (b), respectively, but for the region north of the Bahamas. 64
26 Surface velocity in the proximity and at the Florida Straits for experiment Prel-E03 at: (a) day 161, (b) day 210, (c) day 273, and (d) day 336. 65

List of Tables

1 Parameters defining configuration of vertical layers on the grid used in this study. 41
2 Set of experiments proposed in this study. 42

1 Introduction

The Florida Current (FC) is the westen boundary current closing the subtropical gyre circulation in the North Atlantic Ocean. Unlike other western boundary currents, the FC carries both the return flow associated with the wind-driven gyre and the upper branch of the Meridional Overturning Circulation (MOC). The total transport associated with the FC is 32 Sv (1 Sv = 10^6 $m^3.s^{-1}$), from which about 20 Sv are generally associated with the wind-driven gyre, and about 12 Sv with the North Atlantic MOC [e.g *Stommel*, 1958; *Atkinson et al.*, 2010]. In addition to the FC, the western boundary circulation associated with North Atlantic's subtropical gyre is also composed by the northward flowing Antilles Current carrying 3-5 Sv [*Olson et al.*, 1984; *Lee et al.*, 1990], and by the southward flowing the Deep Western Boundary Current (DWBC) carrying 26 Sv [*Bryden et al.*, 2005; *Johns et al.*, 2008].

Most of the FC flow has its origin in the Loop-Current, which transport Caribbean waters into the Gulf of Mexico through the Yucatan Channel, and then to the Florida Straits, with transport estimates ranging between 24 to 28 Sv [*Johns et al.*, 2002; *Sheinbaum et al.*, 2002]. Other important sources for the FC flow originate in Old Bahama Channel north of Cuba, and in the Northwest Providence Channel within the Bahamas Archipelago, where previous studies suggest a contribution of $\sim$1.5 Sv [*Johns et al.*, 2002], and of $\sim$1.4 Sv [e.g. *Beal et al.*, 2008], respectively. The FC continues flowing through the Florida Straits, and along the east coast of United States (US), until it detaches from the coast at Cape Hatteras ($\sim$35N), feeding into the Gulf Stream.

The FC/Gulf Stream is one of most widely observed and studied western boundary currents in the world. Particular attention has been dedicated to this current because it carries the upper branch of the MOC, corresponding to an important component of the climate system. In addition, the FC has been also linked with significant changes in sea-level along the east coast of US [*Ezer*, 2013; *Ezer and Atkinson*, 2014], giving it an added level of relevance for consideration by decision makers dealing with coastal resilience. Therefore, given its large importance for earth's climate system, studies aiming to improve the

understanding of the different mechanisms and processes driving the variability of this current in different frequencies are of ultimate relevance.

The FC shows large temporal variability over the record. Measurements at the Florida Straits showed that changes in the FC transport can be as large as 10 Sv between the high and low values [*Schott et al.*, 1988]. Among the different components linked with the FC variability, particular interest was dedicated to the the annual cycle exhibited by the FC transport, which is generally characterized as having an amplitude of 4 Sv, with maximum transport in July [*Niiler and Richards*, 1973]. Using a 16 years record of continous volume transport measurements at the Florida Straits, *Baringer and Larsen* [2001] reported substantial year-to-year changes in the characteristics of the seasonal variability. Year-to-year changes in the seasonality of the FC were further confirmed by *Meinen et al.* [2010] using a longer record of 26 years. While there is general agreement that the annual cycle is forced by a combination of along-channel winds with wind stress curl upstream (Caribbean) and downstream (Gulf Stream) from the Florida Straits [*Schott et al.*, 1988], little is known about other components driving seasonal variability of the FC. Recent findings [*Czeschel et al.*, 2012; *Frajka-Williams et al.*, 2013; *Domingues and Baringer*, 2015] showed that westward propagating signals coming from the ocean interior could potentially drive a significant source of variability for the FC on seasonal time-scales. Because observations [*Molinari et al.*, 1990] and results from numerical models [*Böning and Budich*, 1991] indicate that the seasonal changes in FC transport are linked with seasonal variability in the Meridional Heat Transport in the Atlantic Ocean at 26°N, understading the different components of the seasonal variability of this current is important.

This study aims to improve the understanding of the FC seasonal variability by assessing the forcing mechanisms linking westward propagating signals with changes in the FC transport. This proposal is organized as follows: in section 2, additional scientific background and motivation for this study is described, including a more detailed background on FC variability (section 2.1), and on westward propagating signals (section 2.2); section lists the scientific questions that will guide the development of this study; in

section 4, the proposed work and methods adopted in this study are explained; section 5 assesses results from preliminary experiments developed here; and section 6 summarizes the main findings and lessons learned from these preliminary experiments.

2 Scientific Background

2.1 Variability of the Florida Current transport

Unlike other western boundary currents, the FC has been continuously monitored since 1985 at the Florida straits using telephone cables between Florida and the Bahamas (Figure 1). The cable-derived FC transport time-series relies on simple, yet robust, electromagnetic principle: seawater is an efficient electrical conductor, which implies that water motion in the oceans are linked with the generation of electromagnetic potentials and currents [*Stommel*, 1948]. Daily volume transport measurements are made available in this region by measuring voltages differences between the two sides of the straits. Voltage measurements are then calibrated to provide transport estimates using *in situ* observations from other platforms, such as based on dropsondes [*Larsen*, 1992]. The FC cable data is made freely available at NOAA's Atlantic Oceanographic and Meteorological Laboratory website (`http://www.aoml.noaa.gov/phod/floridacurrent/`).

The FC transport time-series derived from the telephone cables is a continuous record (gray line, Figure 2a) that enabled numerous studies on the different spectral characteristics of this western boundary current [e.g. *Baringer and Larsen*, 2001]. For example, *Meinen et al.* [2010] used the FC transport record during 1982-2008 combined with measurements from other *in situ* instruments to quantify the contribution of different time-scales to the total variability of the FC transport, reporting that: (i) 46% of the variability was in the 1-11 month frequency band, (ii) 24% was in the sub-month band, (iii) 13% was in the 13-42 month band, (iv) 9% was in the annual band, and (v) 8% was linked with periods larger than 42 months. Below, an updated analysis of the FC transport variability is provided for the period between 1985-2013.

During 1985-2013, the FC transport (Figure 2a) exhibits an average volume transport of $\sim$32 Sv (1 Sv = 10^6 m^3s^{-1}), with root mean square (RMS) variability of 3.4 Sv. The transport also shows a climatological annual cycle characterized by high transports ($\sim$34 Sv) from July to September, and low transports ($\sim$30 Sv) from November to January (black line, Figure 2b). The wavelet transform of the FC transport time-series (Figure 2c) indicates that the FC is linked with variability in different frequency bands, and that there were significant changes in the spectral characteristics of this current throughout the record. Variability significant at the 95% confidence interval is observed for: (a) the high-frequency band with periods smaller than 73 days; (b) an intermediate frequency band with semi-annual and annual periods within the 73-525 days range; and (c) the low-frequency band with two-year periodicity. The wavelet diagram also suggests the presence of 5 year periodicity in the FC transport time-series, however, longer records are needed to confirm the statistical significance of this signal. It is quantified here that the total variability of the FC transport during 1985-2013 is accounted by: (i) 53% due to high-frequency variability ($<$73 days, RMS = 2.5 Sv); (ii) 35% due to changes in transport within the 73-525 day frequency band (RMS = 1.9 Sv); and 12% due to low-frequency variability ($>$ 525 days). The transport variability within the 73-525 day frequency band may be further decomposed as: 8% due to the climatological annual cycle of this current; and 27% due to seasonal variability linked with variable annual phase, previously defined as the transient seasonal component [*Domingues and Baringer*, 2015].

Different studies addressed the seasonal variability of the FC transport, with particular focus on the climatological annual cycle exhibited by transport measurements across the Florida Straits (Figure 2b). The FC annual cycle was first described based on 90 dropsonde transects during 1964-1970 as having an amplitude of 4 Sv (1 Sv = 10^6 m^3 s^{-1}), with maximum transport in July [*Niiler and Richards*, 1973]. Later studies confirmed the statistical significance of the annual cycle based on the continuous FC record derived from cable measurements [*Baringer and Larsen*, 2001; *Meinen et al.*, 2010]. There is general agreement that the annual cycle of the FC is driven by a combination of along-channel winds with

wind stress curl upstream (Caribbean) and downstream (Gulf Stream) from the Florida Straits [*Schott et al.*, 1988]. Changes in along-channel winds drive anomalous eastward Ekman transport, leading to adjustments in the pycnocline and pressure gradients across the straits [*Schott et al.*, 1988; *Rousset and Beal*, 2011]. Changes in the upstream/downstream wind stress curl are linked with the generation of barotropic waves that can reach the Florida Straits and adjust the flow of this current within one month [*Czeschel et al.*, 2012].

Even though the FC exhibits a statistical annual cycle linked with the wind forcing, the annual cycle accounts for only 8% of the total FC variability, and seasonal changes recorded for a specific year may exhibit highly anomalous patterns (Figure 2b). For example, while in 1989 an amplified annual cycle with similar phase was observed, a 90° phase displacement in the annul cycle was recorded in 1986, and even a semi-annual cycle in 1998. Changes in the annual behavior of the FC were first acknowledged by *Baringer and Larsen* [2001], who reported that the seasonal variability during 1982-1990 (annual cycle) was substantially different from the variability during 1991-1998 (semi-annual cycle). Additional changes in the FC seasonal variability were also reported for the period during 2001-2007, which was characterized by an annual cycle having a weak semi-annual component, and with small changes in phase [*Meinen et al.*, 2010]. Based on these observations, *Meinen et al.* [2010] suggested that different processes, other than the wind forcing, may drive the observed interannual changes in the FC seasonal variability. Indeed, more recent studies showed that the local eddy field [*Frajka-Williams et al.*, 2013] and baroclinic signals coming from the interior [*Czeschel et al.*, 2012] may drive changes in the seasonal variability of the FC.

Interannual changes in the FC seasonal variability are linked with the transient seasonal component (blue line, Figure 2a), which contributes 27% to the total FC variability. Observations analyzed by *Domingues and Baringer* [2015] showed that westward propagating signals coming from the interior largely explain the variability exhibited by the transient seasonal component of the FC transport. However, a better understanding of the response generated by these signals at the western boundary is still required, and this

study aims to fill this gap. In the following section (section 2.2), westward propagating signals in the North Atlantic within the 73-525 day frequency band are introduced and characterized.

2.2 Westward propagating signals in the North Atlantic

In this section, the characteristics of westward propagating signals in the North Atlantic are assessed. The characteristics described here will be used as background information for designing the numerical experiments developed in this study (Section 4.1).

Westward propagating signals or waves arise as solutions for the linearized quasi-geostrophic equations of motion when the latitudinal-dependency of the Coriolis parameter (e.g. the β term) is considered. For example, solutions of the type of first-mode baroclinic Rossby waves may be obtained from the linearized equations of motions considering small perturbations on one-and-a-half layer ocean model. In this model, the propagation of perturbations follows the dispersion relation for first-mode baroclinic Rossby waves:

$$\omega = \frac{-\beta k}{k^2 + l^2 + {R_d}^{-2}} \qquad \text{, and} \qquad C_p = \frac{\omega}{k} \tag{1}$$

where β indicates variations of the Coriolis parameter with latitude, k is the zonal wave number, l is the meridional wave number, R_d is the first-mode radius of deformation, and C_p is the zonal phase speed. Figure 7 shows the dispersion relation for first mode, baroclinic rossby waves at 27°N using mean temperature and salinity profiles from the World Ocean Atlas 2013 [*Locarnini et al.*, 2013; *Zweng et al.*, 2013] for the region between 82°W and 61°W, and 22°N and 37°N, which correspondx to the area where numerical experiments are developed in this study (see section 4.2).

Even though westward propagating signals may be described by relatively simple dynamics, they are largely observed in the real oceans using satellite-derived sea height anomaly (SHA) data from altimetry [e.g. *Oliveira and Polito*, 2013], and using sea surface temperature (SST) data [e.g. *Halliwell Jr et al.*, 1991]. Previous studies using SHA

data [*Polito and Liu*, 2003] showed that westward propagating signals behaving like first-mode baroclinic Rossby waves account for a large component of the SHA variability in the global oceans. Because SHA data provides overlaid signals from first-mode baroclinic Rossby waves and from nonlinear westward propagating mesoscale eddies, the generic term "westward propagating signals" [*Oliveira and Polito*, 2013] is adopted here.

Polito and Liu [2003] reported that westward propagating signals with semi-annual and annual timescales contribute most of the SHA variability in the North Atlantic. In the following analysis, westward propagating signals are characterized for the 73-525 days frequency band, which corresponds to the combined semi-annual and annual waves described by their study. A brief quantitative assessment on the role of these signals in the upper-ocean variability in the subtropical region of the North Atlantic is also described. To accomplish this, weekly fields of gridded SHA with $^{1/4}$degree horizontal resolution are obtained from AVISO's (Archiving, Validation and Interpretation of Satellite Oceanographic data) delayed-time database for the period of 1993-2013 (available at: `http://www.aviso.oceanobs.com`).

Satellite-derived SHA anomaly data shows variability in different time and spatial scales in the North Atlantic. At 27°N, the latitude of the Florida Straits, SHA is linked with RMS variability of ∼5cm close to eastern boundary, which increases westward to ∼13cm at 76°W, and decrease rapidly to ∼7 cm at the western boundary (blue line, Figure 3). The rapid decline in the SHA RMS values, or in the eddy variability, at the western boundary is further discussed below. Another important component of the SHA variability is due to a well-defined annual cycle during 1993-2013 (not shown here) that is obtained by calculating weekly averages during 1993-2013. This component is generally linked with the steric variability of sea-level [*Guinehut et al.*, 2006]. The RMS linked with the SHA annual cycle shows small changes in the zonal direction, with values ranging between $\sim$ 3 cm and $\sim$ 5cm (red line, Figure 3). It is estimated here that this component contributes 21% of the total SHA variability at 27°N west of 60°W (60°W corresponds to the eastern limit for numerical experiments developed in this study, Section 4.1). After re-

moval of the annual cycle, filtered SHA at the 73-525 days frequency band (SHAr) show RMS values ranging between $\sim$ 2 cm at the eastern boundary and $\sim$ 7 cm at 76°W, displaying a rapid decline west of 76°W. The SHA variability at the 73-525 days frequency band accounts for 42% of the total SHA variability west of 60°W. The low-frequency (periods $>$ 525 days) and high-frequency (periods $<$ 73 days) components show RMS values of $\sim$ 2 cm in the interior (green and gray lines, Figure 3). Close to the western boundary, the high-frequency component show values as large as $\sim$ 6 cm. The low-frequency and high-frequency components contribute 12% and 25% to the total SHA variability west of 60°W, respectively. From now on, focus is given to the SHA variability in the 73-525 days frequency band, which corresponds to the combined semi-annual and annual westward propagating signals studied by *Polito and Liu* [2003], and to the same frequency band linked with the transient seasonal variability of the FC transport described above. As reported here, the 73-525 days frequency band is the main component of the SHA variability west of 60°W. This frequency band also includes first mode, linear, baroclinic rossby waves, which have a cutoff period and wavelength of 153 days and 293 km, respectively, for the shortest westward propagating wave (Figure 7).

After removal of the annual cycle, SHAr exhibits an eddy-like spatial signature in the North Atlantic (e.g., SHAr on March 1st, 2000, Figure 4), with values ranging between -15 cm and 15 cm at 27°N, and values larger than (smaller than) 20 cm (-20 cm) north of 35°N linked with the Gulf Stream extension. Similar eddy-like westward propagating signals with time-scales similar to the one reported here were also previously identified in this region using SST data [*Halliwell Jr et al.*, 1991]. The westward propagation associated with these features is identified by the sloping SHA pattern using a a hovmoller (longitude-time) diagram of SHAr (e.g., at 27°N, Figure 5a), which indicates that signals travel with phase speed of approximately -4.6$\pm$ 1.4 km day^{-1} at 27°N. Phase speeds estimated here are consistent with previous values reported by other studies in the North Atlantic based on SHA [*Polito and Liu*, 2003], and SST [*Halliwell Jr et al.*, 1991] data. Westward phase speeds from standard linear theory for first baroclinic Rossby waves can be estimated

using real ocean data; in the long wave limit, the dispersion relationship and derived zonal phase speed (Equation 1) may be simplified in the form of:

$$C_p = -\beta R_d^2 \qquad \text{, where} \qquad R_d = \frac{c_1}{f} \tag{2}$$

In this equation, f is the Coriolis parameter, and c_1 is first mode speed. Estimates of c_1 can be obtained by solving the modal equation numerically:

$$\phi_n(z) = -{c_n}^2 \frac{\partial}{\partial z}\left(\frac{1}{N_s^2}\frac{\partial \phi(z)}{\partial z}\right) \tag{3}$$

where $\phi_n(z)$ provides the vertical structure of mode n, c_n is the modal speed, and N_s is the buoyancy frequency. Figure 6 exhibits values of C_p and R_d calculated for the North Atlantic using climatological temperature [*Locarnini et al.*, 2013] and salinity [*Zweng et al.*, 2013] fields from the World Ocean Atlas 2013. Analysis of C_p indicates that phase speeds predicted by standard linear theory at 27°N (-3.5$\pm$ 0.4 km day^{-1}) are approximately 30% slower than westward propagating signals revealed by satellite altimetry. Indeed, ocean observations generally show westward phase speeds faster than values predicted by standard theory [e.g. *Chelton and Schlax*, 1996; *Killworth et al.*, 1997; *Oliveira and Polito*, 2013], which is in part because potential vorticity gradients induced by background baroclinic flows in the real ocean are neglected in the standard linear theory [*Killworth et al.*, 1997]. However, the evaluation of these mechanisms is beyond the scope of this work.

The power spectrum density obtained from a fast fourier transform of SHAr time-series show the intensification of the spectral power towards the western boundary (Figure 5b). This indicates an increase in the eddy energy towards the western part of the basin. The power spectrum density also shows a rapid decay in the spectral energy west of 76°W, which coincides with the rapid decline in the SHA RMS close to the western boundary described above. A similar decline in the SHA RMS (or eddy variability) close to the western boundary has been previously observed by *Kanzow et al.* [2009], who proposed a mechanism to explain this observation: because normal velocities are not admitted through the boundary, along-boundary pressure gradients are not sustainable, caus-

ing pressure anomalies to propagate quickly there. This mechanism causes a rapid decay of the eddy energy near the western boundary, which is transmitted equatorward at western boundary regions. Improving the understanding of such mechanisms at the western boundary region of the North Atlantic is one of the motivations for this work, as will be detailed below (Section 3).

To evaluate the wavelengths linked with westward propagating signals within the 73-525 day frequency band in the North Atlantic, a similar analysis using a fast-fourier transform is applied by transforming the SHAr data from spatial coordinates to wavenumber space. This analysis shows that westward propagating signals at 27°N are linked with a broad band spectrum of wavelengths, with increasing energy to about 300 km, and then flat to longer wavelengths (Figure 5c).

2.3 Eddy-related variability at North Atlantic's western boundary

Evidence suggesting the influence of westward propagating signals in the variability of the western boundary current system in the subtropical North Atlantic has been long shown by *in situ* observations in the region. At the Florida Straits, early observations showed that the overall transport variability observed within individual cruises was comparable and even greater than levels of variability associated with the annual cycle shown by this current [*Leaman and Molinari*, 1987a; *Leaman et al.*, 1987b]. These studies reported that transport variability on seasonal time-scales was partially associated with meandering of the FC, and with intermittent signals coming from the Northwest Providence Channel.

The Northwest Providence Channel corresponds to the main passage connecting the Florida Straits with the western boundary region east of the Bahamas (Figure 1), where strong variability on seasonal time-scales is also generally observed [e.g. *Lee et al.*, 1990, 1996; *Bryden et al.*, 2005; *Johns et al.*, 2008]. Observations from current measurements during April 1987 to June 1988 by a mooring array east of Abaco, Bahamas, exhibited variability dominated by periodic events occurring every 100 days associated with anticy-

clonic features centered northeast of the Bahamas [*Lee et al.*, 1990]. Further analysis by *Lee et al.* [1996] showed that the variability in the upper 800 m east of Abaco was dominated by westward propagating wavelike baroclinic eddies at mean periods of 30 and 100 days, with wavelengths of approximately 230 and 335 km, respectively. Their study also reported that meridional transport anomalies were linked with strong offshore-onshore meandering of the DWBC east of the Bahamas that could potentially mask the wind-driven annual cycle in the region. The core of the DWBC tended to shift offshore as these westward propagating baroclinic signals interacted with the western boundary at the Bahamas escarpment.

The numerical simulations developed by *Böning and Budich* [1991] on a $^{1/3}$ degree grid provided one of the earliest model-based results showing evidence of the influence of westward propagating baroclinic signals on the the western boundary currents in the North Atlantic on time-scales of 80-120 days. The response simulated by their numerical experiments was generally in good agreement with observations, showing that the wind-driven annual cycle of meridional volume transports east of the Bahamas was masked by strong transport fluctuations with time-scales of 100 days associated with baroclinic signals coming from the interior. Another study on the North Atlantic [*Czeschel et al.*, 2012] based on a adjoint model approach showed that westward propagating baroclinic signals coming from the interior corresponded to a relevant component of the FC annual variability. According to their study, the FC annual variability is driven by both: (a) the wind forcing north of the Florida Straits, which causes a fast barotropic adjustment in the current with amplitude of $\sim$1 Sv; and by (b) long baroclinic Rossby waves coming from the interior, which force a $\sim$0.8 Sv adjustment in the FC transport with different annual phase.

Recent studies based on *in situ* and SHA observations from satellite-altimetry provided additional insight on the eddy-induced variability at the western boundary current system in the North Atlantic. In one study [*Frajka-Williams et al.*, 2013], coincident fluctuations in Antilles Current and Florida Current transports were found to be associated

with anticyclonic features east of the Bahamas. Their results showed that anticyclonic eddies with diameters of 200 km - 300 km and amplitudes of $\pm$ 15 coming from the interior could potentially drive a relevant component of the transient seasonal variability of the western boundary current system in the North Atlantic. Another study [*Domingues and Baringer*, 2015], focused on the seasonal variability of the FC, quantified that changes in sea-level along the coast linked with westward propagating signals coming from the interior accounted for $\sim$50% of the FC transient seasonal variability. According to their results, the transport in the Florida Straits "feels" integrated changes in sea-level along the coast caused by westward propagating signals impinging on the western boundary within different latitude bands between $\sim$26.5°N - 42.0°N.

Results from the studies described above provide valuable evidence of the variability induced by westward propagating signals on the western boundary current system in the subtropical North Atlantic. However, a better understanding on the mechanisms driving the response at the western boundary is still required. In the next section (Section 2.4), some of the mechanisms driving the eddy/western boundary interaction are assessed from studies based on idealized analytical and numerical simulations.

2.4 Eddy-wall mechanisms

Even though westward propagating signals behaving like first baroclinic Rossby waves have been widely observed in real oceans [e.g. *Halliwell Jr et al.*, 1991; *Polito and Liu*, 2003; *Oliveira and Polito*, 2013], isolating their response at western boundary regions can be very challenging. This is because these regions are characterized by highly nonlinear dynamics due to the presence of intense background flows and high-levels of eddy kinetic energy (EKE). The inherent nonlinear dynamics in western boundary regions implies that processes occurring on various temporal and spatial scales can interact, making it hard, or nearly impossible in some cases, to isolate signals linked with specific processes. For example, *Byrne et al.* [1995] tracked westward propagating eddies shed by the Agulhas Current in the South Atlantic, and found that identifying their signal in regions close to

the western boundary was complicated by the presence of the Brazil Current. Therefore, previous studies relied on simplified dynamics and idealized numerical experiments to investigate the response generated by westward propagating eddies and other signals at the western boundary, focusing mainly on: (a) the evolution of pressure anomalies (dynamic height) along the boundary; and on (b) the fate of the eddy itself. In this section, the underlying dynamics and main outcome from these experiments are summarized.

The study by *Milliff and McWilliams* [1994] focused on the evolution of pressure anomalies along the boundary of ocean basins given an initial perturbation in the ocean interior. They used two numerical models based on the shallow water equations and on the quasi-geostrophic equations initialized with a monopole vortex (anticyclone) of 200 km diameter on a rectangular, and flat-bottom ocean basin. Some of the main results reported by their study include: (1) the westward propagation of the vortex at a rate consistent with the dispersion of Rossby waves; (2) the development of a Rossby wave field on the wake of the vortex; (3) the development of coastally trapped waves when the vortex encountered the boundary; (4) the scattering of signals from coastally trapped waves along the meridional boundary; (5) the completion of vortex-boundary interaction after 120 days of simulation; and (6) residual variability at the western boundary after 120 days caused by westward propagating Rossby waves that developed on the wake of the original vortex. Their experiments provided a mechanism coupling the short time-scales motions in the coastal waveguide with longer time-scale motions at the ocean interior. Similar results were also found by *Kanzow et al.* [2009] using a nonlinear one-and-a-half layer reduced-gravity model in a rectangular, flat-bottom ocean basin. Their results also showed that these boundary-trapped waves cause the observed decline of sea-level variability along the coast, once they provide the mechanism for the fast export of transport anomalies equatorward due to eddies impinging on the western boundary.

With respect to the fate of the eddy once it reaches the western boundary, previous studies by *Nof* [1988] and *Nof* [1999] provided a detailed analysis of mechanisms and time-scales involved using a nonlinear, inviscid one-and-a-half layer model. Based on an-

alytical and numerical experiments initialized with a zero potential vorticity anticyclonic eddy ($\partial u/\partial y = f$), they reported that: (1) as the ring moves into the wall, it gradually leaks its content equatorward along the boundary until it loses all of its mass, like a peeling onion; (2) the "peeling" rate is $2\beta R_d^2/9$, implying that the eddy migrates towards the wall at a rate that is one-third of the free open ocean rate controlled by the dispersion of Rossby waves; (3) upon contact with the western boundary, anticyclonic eddies tend to stay at a fixed latitude due to two sub-processes in approximate balance, the (a) β equatorward tendency, and (b) the rocket effect, which causes a poleward tendency due to the equatoward leakage of the eddy along at the wall. According to their study, a typical intense eddy would take $\sim$200 days to "leak" 70% of its volume. Even though they acknowledged that identifying such mechanisms in the real oceans would be difficult, they suggested that similar processes may occur in various western boundary regions, such as at the Gulf Stream.

An additional case considered by *Simmons and Nof* [2002] was the interaction of eddies that encountered porous western boundaries regions, such as the islands of the Lesser Antilles in the tropical North Atlantic. To accomplish this, they developed sets of experiments using different boundary configurations on the same model as *Nof* [1999]. Their results revealed that: (1) throughout the encounter with the porous boundary, eddies remained axisymmetric while being drained by wall jets; (2) while leaking, the eddy diameter ultimately adapted to the gap width, so that it would lose contact with the walls and drift slowly into the interior of the western basin; (3) in the multiple gap problem, all the fluid from the approaching eddy penetrated into the interior of the western basin, in contrast to most of the single gap problems; and that (4) eddies that encountered large islands showed a tendency to break into smaller offsprings. They also showed that even large eddies can pass their volume through narrow passages, estimating that 85% of the content from a anticyclonic eddy with 280 km diameter would be able to flow through a passage 80 km wide. Their results indicate that the signal from eddies and other mesoscale features can efficiently cross islands arcs, such as the Bahamas archipelago.

The western boundary region in the subtropical North Atlantic has some characteristics that are similar to configurations used on the experiments described above, such as the combination of a solid wall (steep slope) north of 27°N, and a porous wall south of 27°N due to the Bahamas archipelago. Therefore, similar responses may be observed at the North Atlantic's western boundary, to some extent. While these studies provided insight on the mechanisms linked with eddy-wall interactions based on highly idealized experiments, in this study we take a further towards understanding the variability induced by westward propagating signals at the western boundary region in the subtropical North Atlantic by performing sets of controlled realistic high-resolution numerical experiments (Section 4.2).

3 Questions

The goal of this study is to improve the understanding of the FC transient seasonal variability. To accomplish this, we intend to address the following questions:

(Q1) Can westward propagating signals drive transport variability on seasonal timescales (73-525 day) at the Florida Straits?

(Q2) What are the mechanisms driving the response at North Atlantic's western boundary?

(Q3) How is the response different for anticyclonic and cyclonic eddies?

(Q4) What is the vertical structure of the responses induced at the Florida Straits?

(Q5) How do westward propagating signals in different latitude bands contribute to the variability at the Florida Straits?

(Q6) How does the background FC flow modulate the response at the western boundary?

(Q7) Can these signals induce variability in other frequency bands (e.g. long-term variability)?

4 Proposed Work

In this study, we will simulate in detail the response generated by westward propagating signals at the western boundary in the subtropical North Atlantic. To address the questions listed on Section 3, this study employs a robust approach combining a sophisticated numerical model that enables realistic oceanic simulations (Section 4.1), with controlled experiments based on idealized initial conditions (Section 4.2).

4.1 Regional Ocean Modeling System - ROMS

The research developed here will be based on numerical experiments using the Regional Ocean Modeling System (ROMS, available at https://www.myroms.org/). ROMS consist of a free-surface, terrain-following ocean model that solves the hydrostatic primitive momentum equations on a staggered Arakawa C-grid *Shchepetkin and McWilliams* [2005].

Because ROMS provides a wide range of modules and configurations, it has been widely used by the scientific community, with applications ranging from studies focused on sediment transport at the coast [*Blaas et al.*, 2007] to studies making long-term climate projections [*Ådlandsvik*, 2008]. In this study, the following configuration is used: (i) nonlinear equation of state; (ii) analytical spherical grid; (iii) centered, fourth order advection of tracers and momentum; (iv) harmonic horizontal mixing of tracers and momentum; (v) KPP vertical mixing [*Large et al.*, 1994]; and the (vi) splines density Jacobian for the pressure gradient computation [*Shchepetkin and McWilliams*, 2000]. Boundary conditions for each experiment are described on Section 4.2.

4.2 Numerical experiments

Experiments developed in this study are carried out in a domain within 60°W - 82°W, and 21°N - 37°N (Figure 8). The grid used for numerical simulations has an horizontal resolution of approximately $^{1/25}$degree, with 540 X 390 points in the longitudinal and latitudinal direction, respectively, and 30 vertical layers. The bottom topography is derived from ETOPO-1 [*Amante and Eakins*, 2009], with the maximum grid stiffness controlled by setting the Beckman & Haidvogel parameter (rx0) to 0.1, and the Haney parameter (rx1) to 2.7. These configurations of rx0 and rx1 are selected to avoid spurious and unrealistic flows resulting from pressure-gradient errors [*Beckman and Haidvogel*, 1993; *Haney*, 1991]. Because this research focuses on the response of the FC driven by westward propagating signals arriving at the western boundary, realistic bottom topography is used at and in the proximity of the east coast of the United States (Figure 8a,b). The bathymetry at the ocean interior, on the other hand, is simplified by setting the maximum depth to 5000 m, and by enforcing flat-bottom conditions west of 70°W. Parameters describing the configurations of vertical layers are available on Table 1.

Different sets of experiments are developed in this study (Table 2), which were designed to directly address the questions listed on Section 3. For all experiments, flat-isopycnal conditions are imposed in the domain by applying the average temperature, salinity, and density profiles (Figure 9a,b,c) from the World Ocean Atlas 2013 [*Locarnini et al.*, 2013; *Zweng et al.*, 2013] for the region corresponding to our domain. Flat-isopycnal conditions are initially prescribed everywhere in the domain to ensure stationary initial conditions, removing background baroclinic flows that are intrinsic to real-ocean climatological fields (e.g due to horizontal density grandients). Numerical experiments are then developed using initial conditions constructed using different configurations of westward propagating signals prescribed as small perturbations in the pycnocline depth in the ocean interior. Additional information describing the method for including westward propagating signals in initial condition fields are provided in section 4.3. All experiments are also developed in the absence of wind forcing, in order to isolate the response driven

by westward propagating signals in the variability at the western boundary region. An indirect outcome of this condition imply in the absence of background flows associated with the Antilles Current, which is largely associated with the return flow for the wind-drive gyre circulation [*Lee et al.*, 1990].

The first few set of experiments are developed in the absence of the FC flow to enable an initial understanding on the responses generated by westward propagating signals impinging along the east coast of United States. Later, experiments are developed with the FC to evaluate the role of the background flow from this current in modulating the responses at the western boundary.

In the set of experiments designated ARCR-E0x, numerical simulations are initialized without the FC and with single anticyclonic or cyclonic eddies at different latitudes. With this set of experiments, we hope to: identify the mechanisms driving the response at the western boundary (Q2); analyze differences in the response driven by anticyclonic eddies and by cyclonic eddies (Q3); and also to evaluate the vertical structure associated with the different responses at the western boundary (Q4).

In the set of experiments designated EdFul-E0x, simulations are initialized with constant inflow of westward propagating signals using altimetry data as boundary conditions. Inflow of eddies through different latitude bands will be simulated to evaluate the relative contribution of eddies impinging in different locations along the boundary for driving variability at the Florida Straits (Q5); and also to investigate if the interaction of eddies can lead to variability in the Florida Straits on a broader frequency band, such as on year-to-year time-scales (Q7).

The set of experiments designated ModFC-E0x will be equivalent to experiments on ARCR-E0x, but this time with the background flow of the Florida Current. With this analysis, we intend to understand how the background flow of the FC modulates the response at the western boundary (Q6). Similarly, the set of experiments designated LTerm-E0x is also equivalent to EdFul-E0x experiments, but this time with the FC flow. This set of experiments will enable the evaluation of changes in the FC flow on a broad range of

frequencies that are induced by signals originated in the ocean interior. The full list of experiments developed in this study is given in Table 2.

In this proposal, results from preliminary experiments Prel-E01, Prel-E02, and Prel-E03 are presented on section 5. Experiments Prel-E01 and Prel-E03 are initialized with single anticyclonic eddies included at 27°N/71°W and 29°N/76°W, respectively Experiment Prel-E02 is initialized with a train of cyclonic and anticyclonic eddies at 27°N. The analysis of these preliminary experiments will give insight on the potential responses at the western boundary, and will also help to establish the analysis performed in this study.

4.3 The feature model approach

This section describes the technique used for introducing different configurations of westward propagating signals in our simulations. As described in section 2.2, westward propagating signals with seasonal time-scales in the North Atlantic were characterized as eddy-like features with broad band spectrum dominated by wavelengths of 300 km and larger (27°N). They were also associated with RMS SHA variability of $\sim$7 cm, indicating that during 95% of the time their sea-level signature have values ranging between -14 cm and 14 cm, assuming a normal distribution. These characteristics are used as background information for including westward propagating signals in our modeling experiments.

As mentioned on section 4.2, westward propagating signals are prescribed in initial condition fields as perturbations in the pycnocline depth. To accomplish this, we rely on concepts introduced by the feature model approach [*Robinson et al.*, 1988], which consists in creating oceanographic features of interest using mathematical functions [*Calado et al.*, 2008]. In the past decades, the feature model technique has been employed on early ocean forecasts systems as a alternative to the scarse availability of real-ocean data [*Fox et al.*, 1992].

In this study, eddy-like perturbations on isopycnal surfaces are constructed using two functions: (i) a gaussian function (G_{xy}, Equation 4) and (ii) a modified first baroclinic mode for vertical velocity ($\phi_{1_m}(z)$, black line, Figure 9e). The gaussian function G_{xy} de-

fines the horizontal structure and magnitude of isopycnal displacements, and is calculated according to the following formula:

$$G_{xy}(x) = \Delta z_{max} \times exp\left(\left\{-\frac{2xe}{D_E}\right\}^2\right), \qquad \text{with } x \propto \left[-\frac{D_E}{2}, \frac{D_E}{2}\right] \tag{4}$$

In this equation, the parameter D_E defines the horizontal diameter of the eddy, and Δz_{max} sets the maximum vertical displacement of the pycnocline depth. If Δz_{max} is negative, perturbations on isopycnal surfaces will lead to an anticyclonic eddy, while a positive Δz_{max} will lead to a cyclonic eddy. Figure 10 provides a schematic view of G_{xy}.

The modified first baroclinic mode for vertical velocity is used to define the vertical structure of the vertical displacement of individual isopycnal surfaces. The original (rigid-lid) first baroclinic mode (gray line, Figure 9e) is obtained solving Equation 3 using the mean temperature and salinity profiles (Figure 9a,b) for the domain. $\phi_{1_m}(z)$ is then calculated by adding a linear profile with maximum value of 0.5 at the surface and minimum value of 0 at ∼1300 m, which is the depth associated with the maximum value observed for this mode. This modification on $\phi_1(z)$ is perfomed to enable the development of surface velocities and free-surface signals, which would be otherwise flat if using the original mode based on a rigid-lid approximation. Vertical perturbations on isopycnal surfaces are ultimately achieved using:

$$\frac{\partial \rho}{\partial t} = -w\frac{\partial \rho}{\partial z} \tag{5a}$$

$$\rho' = -\left(w\Delta t\right)\frac{\partial \rho}{\partial z} \tag{5b}$$

$$\rho' = -\left(\Delta Z\right)\frac{\partial \rho}{\partial z} \tag{5c}$$

where ΔZ is obtained as:

$$\Delta Z(x,z) = G_{xy}(x) \times \phi_{1_m}(z) \tag{5d}$$

Figure 11 shows an example of the temperature, salinity, and density structure of a single anticyclonic eddy prescribed at 27°N and 70.5°W using D_E equal to 150 km and Δz_{max} equal to 300 m. These fields are used as initial conditions for preliminary experiment Prel-E01.

After the creation of initial conditions fields, numerical experiments are started from rest on the diagnostic mode, which can be accomplished on ROMS by activating the flag *TS_FIXED*. The diagnostic mode implies the evolution of momentum fields (free-surface, baroclinic and barotropic velocity) with tracers fields (temperature and salinity) held constant. This approach enables the geostrophic adjustment of momentum fields to the perturbations in the pycnocline depths prescribed as initial temperature and salinity conditions; it prevents the partial dispersion of the available potential energy during initialization due to the propagation of internal waves. Experiments are developed on diagnostic mode until the full adjustment of momentum fields to the prescribed perturbations on isopycnal surfaces. The full adjustment can be identified once the domain-averaged kinetic energy levels out, indicating the development of steady-state conditions.

After completion of this step, the geostrophically adjusted momentum and tracers fields are allowed to evolve in time using ROMS on prognostic mode, which is accomplished by deactivating the flag *TS_FIXED*. Snapshots of model solution are saved every 7 days of simulation time. Experiments are integrated for up to 610 days to allow the westward propagation of initial perturbations, and the full interaction of these signals with the western boundary. The response generated at the western boundary driven by impinging westward propagating signals is then analyzed for different experiments.

On preliminary experiments Prel-E01, Prel-E02, and Prel-E03, prescribed eddies have a diameter of 150 km, and carry ∼10 Sv of volume transport above 1000 m. These eddies simulate the smaller wavelengths (∼300 km) observed in the filtered altimetry record for the North Atlantic Ocean at 27°N (Figure 5c). One expected outcome of this initial condition is the generation of short Rossby waves, given that the cutoff wavelength for long rossby waves is 416 km considering symmetrical features (blue line, Figure 7). The

generation of short Rossby waves may partly propagate the available potential energy eastward towards the open boundary. Figure 12 (left column) shows the SSH signature during initialization for these three experiments. It is hoped that the analysis of these preliminary experiments will provide insight on the type of responses generated at the western boundary, and will also establish the baseline for the analysis of future experiments developed in this study.

5 Preliminary Results

In this section, results from preliminary experiments are analyzed. The analysis first addresses characteristics of the experiments regarding initialization and open-ocean processes, and then focuses specific processes/responses forced at the western boundary. Analyses and results presented here will serve as background information for future experiments developed in this study.

5.1 Initialization & Open-ocean Processes

As previously described in Section 4.3, experiments are started from rest on diagnostic mode for a period of 30 days until the full adjustment of momentum fields to initial perturbations in the pycnocline. Figure 13 show the evolution of the domain-averaged kinetic energy for the three preliminary experiments Prel-E01, Prel-E02, and Prel-03. These time-series exhibit an overall increase in kinetic energy levels during the first 10 days overlaid on large high-frequency oscillations that are slowly damped as the experiment evolves. These high-frequency oscillations display well-defined periodicity of $\sim$28 hours, which is within one standard deviation from the average inertial period estimated for the domain (25.1 $\pm$3.7 hours), indicating the influence of inertial motions during the spin-up period. Similar oscillations are not observed in the evolution of domain-averaged kinetic energy for experiment Prel-E01 in the absence of the Corilios term (Figure 13d, ROMS flag *UV_COR* deactivated), which confirms that such oscillations are indeed linked to inertial

processes. It is worth emphasizing that during diagnostic mode simulations, momentum fields are allowed to evolve freely, which enables the development of inertial motions. The tracers fields, on the other hand, are held constant, implying in a constant pressure-gradient forcing. While this forcing term is slowly balanced by the Coriolis force as the momentum fields develop, in the absence of the Coriolis term, momentum fields accelerate until the model blows up after $\sim$12 days (Figure 13d). Time-series of domain-averaged kinetic energy for these three experiments also indicates the development of stable conditions after 20 days of simulation time, suggesting that spin-up of prescribed perturbations is fully achieved for this domain. Adjusted perturbations associate with maximum velocities of magnitude of $\sim$0.5 m.s^{-1} for experiment Prel-E02 (eddy train) and of $\sim$0.4 m.s^{-1} for experiments Prel-E01 and Prel-E02 (single eddy experiments). Future experiments will be also spun up for 30 days in the diagnostic mode to allow full adjustment of momentum fields to prescribed perturbations.

Figure 14 shows the surface velocity, surface relative vorticity, and the vertical velocity structure associated with the spun up eddy prescribed in experiment Prel-E01. Relative vorticity field indicates the presence of a positive vorticity shield around the negative vorticity core associated with the prescribed anticyclone (Figure 14b). The vertical velocity structure also reveals the baroclinic structure of the eddy (Figure 14c). Cumulative transport estimates confirm that prescribed features carry an enclosed upper-ocean transport of $\sim$10 Sv.

After spin-up on diagnostic mode, experiments are released on prognostic mode, implying in the full evolution of momentum and tracers field. The initial stage of preliminary experiments Prel-E01, Prel-E02, and Prel-03 can be summarized as: (1) the westward propagation of perturbations; (2) the development of a rossby wave train in the wake of the vortices; (3) the eastward propagation of the wave packet. The rossby wave train developed in the wake of prescribed perturbations are characterized by zonal scales similar to the initial perturbations, and by elongated meridional scales, resembling the noodle modes observed by *Berloff et al.* [2009], and predicted by linear instability theory. This

characteristic of elongated waves is important for phase propagation, as will be seen later on.

Longitude-time hovmoller diagrams of SSH indicate that signals travel westward along 27°N with phase speed of -2.49±0.26 km.day^{-1} in experiment Prel-E01, and of -2.76±0.21 km.day^{-1} in experiment Prel-E02 (black lines, Figure 15a,b). In experiment Prel-E03, signals travel westward along 29°N with phase speed of -2.17±0.52 km.day^{-1} (black lines, Figure 15c). These phase speeds are ∼35% slower than phase speeds estimated for fastest first-mode baroclinic Rossby waves at 27°N (-3.84 km.day^{-1}) and at 29°N (-3.31 km.day^{-1}), which were calculated using the method described in Section 2.2, and temperature and salinity profiles (Figure 9) imposed in the domain. Longitude-time diagrams also suggest eastward propagation of wave packets, which becomes more evident on results from experiments Prel-E01 and Prel-E02 (Figure 15a,b), once rossby wave signals are observed east of the longitude where initial perturbations were prescribed. Similar results were also reported by a previous study [*Milliff and McWilliams*, 1994] using simpler models based shallow water and quasi-geostrophic equations. This indicates that, despite the more realistic setup employed in this study, propagation of perturbations anomalies in the ocean interior may be successfully described by more simplistic models.

While westward propagation is a prominent feature of modeling outputs for the three preliminary experiments, prescribed perturbations also display meridional motion as they propagate westward. In general, anticyclonic eddies exhibit a tendency for moving southwestward as experiments evolve, while cyclonic eddies in experiment Prel-E02 tend to move northwestward. Meridional motions are linked with conservation of potential vorticity, once initial relative vorticity anomalies prescribed in experiments are partially drained by the rossby wave train (and other processes) that develops on the wake of the vortices. For example, it is estimated here that approximately 40% of the initial perturbation prescribed in experiment Prel-E01 is transferred to the rossby wave train and other mechanisms during the open ocean phase (not shown here). For this experiment, the anticyclonic eddy prescribed at 27°N-70.5°W moves southwestward during model in-

tegration (red dashed-line, Figure 16a) as it conserves potential vorticity along its path (Figure 16b).

Finally, as a natural consequence of westward propagation, prescribed eddies reach the western boundary region after 210 days of simulation time in experiment Prel-E01, 168 days in experiment Prel-E02, and 147 days in experiment Prel-E03. On the next sections, responses generated at the western boundary are assessed.

5.2 Responses at the western boundary

Because the interaction of prescribed eddies with the western boundary display specific characteristics for each of the three preliminary experiments, the analysis developed here addresses each experiment separately.

5.2.1 Experiment Prel-E01

In experiment Prel-E01, the prescribed anticyclone makes initial contact with the western boundary at at 25.5°N-76°W after 210 days of simulation (Figure 17a). Following initial contact, the eddy stays approximately at a fixed location (Figure 12c, Figure 17b) as it is slowly drained along the sloping topography during a period of $\sim$70 days. The eddy volume drained along the topographic slope flows through the passages south of the Northwest Providence Channel. As this process takes place, the eddy diameter and magnitude becomes progressively smaller, until all the eddy volume has leaked through the arc of islands. Inside the arc of islands, modeling outputs exhibit the development of surface velocities anomalies (Figure 17c) reaching values of 0.30 m.s^{-1} on day 266. On this date, the formation of smaller eddies (i.e. offsprings) between the islands is also observed, including one small eddy with diameter of $\sim$50 km that persists for over 200 days east of Andros Island (Figure 17c). The phenomenology behind this response is largely consistent with results reported in a previous study [*Simmons and Nof*, 2002] that addressed the interaction of idealized eddies with arc of island using a non-linear one-and-half layer model model.

While evidence of variability induced by the anticyclonic eddy is seen within the Bahamas archipelago, at the Florida Straits, signals linked with the impinging eddy are not clearly observed. However, time-series of volume transports at the Florida Straits (Figure 18a) indicate the development of velocity anomalies accounting for a meridional transport of $\sim$0.4 Sv around day 231, shortly after the anticyclone makes initial interaction with the western boundary east of the Bahamas Archipelago. Interestingly, transport anomalies at the Florida Straits develop long before the eddy makes initial contact with the boundary region, which suggests the influence of other mechanisms. Analysis of SSH outputs suggests that transport anomalies at the Straits are largely linked with the westward propagating rossby wave field that is associated with the eddy. This result indicates that prescribed eddies generate some band-limited range of Rossby wavenumbers, from which some propagate faster than the eddy. The rossby wave field is associated with broad SSH anomalies that rarely exceed 2 cm. In fact, cross-section velocities at the Florida Straits for day 231 (day of peak transport, Figure 19a) indicate the development of a broad field of northward velocity anomalies with magnitude smaller than 2 cm.s^{-1}. Time-series of volume transports at the Florida Straits (Figure 18a) further exhibit an oscillation with period of $\sim$300 days, which is consistent with time-scales included in the transient seasonal component of the Florida Current. Therefore, preliminary results from experiment Prel-E01 provides initial evidence that the forcing mechanisms discussed by *Domingues and Baringer* [2015] may indeed drive changes in the FC transport.

To further investigate the mechanisms linked with transport anomalies at the Florida Straits, and the fate of westward propagating signals, time-series of SSH are analyzed for locations along the east coast of US (Figure 20a), along the shelf-break (Figure 21a), and at the Bahamas coast (Figure 22a). Latitude-time hovmoller diagram of SSH along the coast and topographic slope for experiment Prel-E01 indicate that SSH anomalies are mostly observed at the Florida Straits (Figure 20b), and slightly north of this region (Figure 21b). Coastal SSH time-series show that peak meridional transport at the Florida Straits on day 231 coincides with increasing SSH at the coast. Peak SSH anomalies at 27°N with val-

ues smaller than 1 cm are observed later, around day 300. Equatorward propagation of SSH anomalies can be identified between 26°N and 25°N during day ∼250 to day ∼450, indicating that signals are transmitted southward along the coast. This latitude-time hovmoller diagram suggests a propagation speed of ∼-0.5 km.day^{-1} (black line, Figure 20b), which is much smaller than speeds expected for first-mode coastally-trapped waves at the east coast of US that are generally $O(1)$ m.s^{-1} (86.4 km.day^{-1}) [*Elipot et al.*, 2013]. Future analysis in this study will address in detail this mechanism.

Comparison of coastal SSH time-series (Figure 20b) with the time-series of meridional volume transport at the Florida Straits further indicates that at zero lag, transport anomalies are only marginally correlated (r=0.5) with SSH anomalies at the coast (black circle, Figure 20c). In this analysis, positive lags imply that coastal SSH anomalies lead transport anomalies, while the opposite holds true. In this sense, large positive correlation coefficients observed at 27°N indicate that transport anomalies lead SSH changes by approximately 100 days, which is consistent with the rate of westward propagation of the Rossby wave field. Similar correlations are observed in the analysis using SSH time-series along the topographic slope instead (Figure 21c). The positive sign of correlation coefficients imply that an increase in transport leads an increase in coastal SSH. On the other hand, the comparison between transport anomalies at the Florida Straits with SSH time-series from the Bahamas (Figure 22a) indicates that changes in transport coincide with positive changes in sea-level at the Bahamas side of the Straits (Figure 22b). This is consistent with the geostrophic dynamics of the response at the Florida Straits. These results indicate that transport anomalies developed at the Florida Straits are more closely related to changes in sea-level at the Bahamas side of the Straits, which then lead to positive changes in sea-level at the Florida coast as signals propagate westward.

5.2.2 Experiment Prel-E02

In experiment Prel-E02, the leading anticyclonic eddy touches the western boundary at 25.5°N-76.3°W on day 147 (Figure 23a). Unlike the behavior exhibited in experiment Prel-

E01, in experiment Prel-E02, the eddy travels northwestward along contours of potential vorticity until it reaches 25.5°N-76.8°W, where it detaches from the sloping topography on day 238 (not shown). At this point, the leading eddy shows moderate eastward motion as it is absorbed by the following anticyclone that approaches the western boundary on day 259 (Figure 23b). The process repeats itself until three anticyclonic eddies merge around day 343 forming a larger anticyclone with diameter of ∼190 km and transport of 3.6 Sv (Figure 23c). The longitude-time hovmoller diagram of SSH (Figure 15b) exhibits the signature of this merging process between days 200 and 400.

The large anticyclone touches the western boundary slightly north of the Northwest Providence Channel entrance at day 357 (not shown). At this time, the eddy stays at an approximate fixed location as it is drained along the topographic slope. Stronger interaction of this eddy with the western boundary, including the Florida Straits, is observed at day 448 (Figure 23d). This interaction continues until day 462, when it detaches from the boundary (not shown). During this time-frame, the eddy diameter reduces to ∼150 km. The volume leaked from the eddy flows through the Northwest Providence Channel until it reaches the Florida Straits, where it drives a jet-like feature with surface velocity anomalies as large as 15 cm.s^{-1} (Figure 23d). This jet integrates an enclosed recirculation feature that connects velocity anomalies at the Northwest Providence Channel, at the Florida Straits, and to the north of the Bahamas Archipelago with the impinging anticyclonic eddy. The development of small-scale eddies with diameters smaller then 50 km within the Northwest Providence Channel is also observed. Similar small-eddies have been previously reported in this area based on real ocean observations [*Leaman and Molinari*, 1987a].

At the Florida Straits, the anomalous jet is associated with a meridional scale of ∼150 km. Cross-section velocities at the Florida Straits for day 448 (Figure 19c) indicates that this jet is linked with northward velocity anomalies at the western part of the section, along the topographic slope, where the core of the Florida Current is generally observed [*Leaman et al.*, 1987b; *Schott et al.*, 1988; *Beal et al.*, 2008]. Northward velocity anomalies are

stronger in the upper 100 m, and occupy the entire water column in the western part of the section. Most of the variability observed at the Florida Straits for this experiment is linked with the development of this feature (Figure 19d).

At the Northwest Providence Channel, westward velocities anomalies of similar magnitude are also observed above 100 m, occupying most of the water column between 25.4°N-25.7°N (Figure 24). North of 25.8°N, cross-section velocities show the signature of the small anticyclonic eddy that formed within the channel. At a later time-frame after day 540, it is also observed the development of a similar anomalous jet, but flowing southward at the Florida Straits, and eastward at the Northwest Providence Channel (not shown). The development of these features is largely linked with the remnants of the enclosed circulation observed at day 448.

Meridional volume transports at the Florida Straits (Figure 18b) indicate that northward anomalies start to develop after $\sim$100 days of simulation; before the leading eddy touches the western boundary. Meridional transports at the Florida Straits exhibit a first peak with value of $\sim$0.7 Sv around day 300, and a secondary peak of $\sim$0.8 Sv close to day 380. During these two occasions, cross-section velocity at the Florida Straits is dominated by a broad field of northward velocity anomalies reaching values as large as 5 cm.s^{-1} (not shown). The development of broad velocities anomalies on this experiment is consistent with results from experiment Prel-E01, which indicates the influence of Rossby wave field.

Analysis of zonal transport time-series across several sections at the Northwest Providence Channel (Figure 25a,b), and north of the Grand Bahama Island (Figure 25c,d) indicates the development of synchronous transport changes in these areas. The orientation of zonal transport anomalies in the Northwest Providence Channel, and north of Grand Bahama Island, and of meridional transport anomalies in the Florida Straits, indicates the development of a large anticyclonic recirculation cell linking the variability in the Straits with the open-ocean. Surface velocity field for day 448 (Figure 23d) depicts the horizontal structure of such recirculation cell.

Transport time-series at the Florida Straits observed for this experiment also suggest a dominant time-scale longer than 400 days. Secondary oscillations in transport also indicate small-period variability of $\sim$100 days. These results suggest that interaction of Rossby waves with signals directly linked with anticyclonic eddies may potentially induce variability in a broader range of frequencies.

Time-series of SSH along the east coast of US (Figure 20d), along the topographic slope (Figure 21d), and at the Bahamas (Figure 22d) are also analyzed here for experiment Prel-E02. Latitude-time hovmoller diagram of coastal SSH (Figure 20d) indicates that north of the Florida Straits, coherent changes in sea-level are seen along the coast. Coherent changes in sea-level along the US coast reproduced by experiment Prel-E02 are consistent with the fast barotropic signals propagating at 128 m.s^{-1} ($\sim$10,600 km.day^{-1}) observed by [*Elipot et al.*, 2013]. At 27°N, SSH signals values of $\sim$0.5 cm are first observed after day 200, which coincides with the time-frame when stronger meridional transport anomalies start to be observed at the Florida Straits (Figure 18b). In fact, for experiment Prel-E02, coastal SSH anomalies are strongly correlated with meridional transport anomalies at the Florida Straits at zero lag (black circle, Figure 20e). This analysis also shows that positive SSH anomalies at the coast lead changes in transport at the Florida Straits, and are then transmitted southward (black line, Figure 20d) at a speed of -0.5 km.day^{-1}, similar to results from experiment Prel-E01. Similar results are also obtained when comparing SSH signals along the topographic slope with transport anomalies at the Florida Straits (Figure 21d). Stronger SSH signals along the coast with values larger than 1 cm are observed after day 400 (Figure 20d), which start decaying around day 500. These stronger SSH signals are linked with the development of the anomalous northward jet at the Florida Straits, which starts reversing around day 500. At the Bahamas, correlation coefficients also indicate that changes in transport coincide with an increase in sea-level at the Bahamas (Figure 22e).

5.2.3 Experiment Prel-E03

In experiment Prel-E03, the anticyclonic eddy is prescribed in a location upstream from the Florida Straits, and closer to the western boundary (Figure 12c). On day 161, this anticyclone makes initial contact with the sloping topography at the western boundary slightly north of 28°N (Figure 26a). Following initial contact, the eddy travels northward along contours of potential vorticity between days 161 and 210, until it reaches 29.2°N (Figure 26b). At this time, the eddy stays at an approximate fixed latitude as it starts leaking along the topographic slope. On day 273, part of the volume leaked by the eddy form a feature (Figure 26c) resembling the wall-jets described by *Nof* [1999]. This feature extends between 26°N and 28°N with a meridional scale of ∼230 km, and is associated with the southward flowing branch of the eddy, whose flow is partially diverted along the boundary. As such, the developed jet flows southward along the boundary with surface velocities reaching values as large as -10 cm.s^{-1}. Cross-section velocities at the Florida Straits (Figure 19e) indicates that stronger flow is observed above 200 m, with southward anomalies occupying the entire water column at the west side of the section. Similar to results from experiment Prel-E02, most of the velocity variability observed at the Florida Straits in experiment Prel-E03 is also linked with the development of this anomalous wall-jet (Figure 19f). The anomalies associated with this jet propagate southward along the western boundary until day 336, when it detaches from the boundary forming a smaller cyclonic feature with diameter of ∼80 km in the proximity of 25°N (Figure 26d).

Time-series of meridional volume transport at the Florida Straits (Figure 18c) exhibit the development of transport anomalies ranging between -0.25 Sv and 0.35 Sv. Southward transport anomalies develop during the first 100 days of simulation, which is then followed by a small period of 61 days dominated by northward anomalies, and again followed by the development of southward anomalies until day 273. Transport anomalies display a dominant periodicity of about 150 days during the first 300 days of simulation, which correspond to the time-frame when eddy is closely interacting with the sloping topography along the coast of Florida. After day 300, northward transport anomalies in-

crease slowly until it reaches the peak value of 0.35 Sv on day 427, implying the existence of longer period variability.

Time series of SSH along the coast (Figure 20f) exhibit the development of small ($\sim$0.2 cm) positive SSH anomalies approximately between days 100 and 200. Stronger negative SSH anomalies reaching values close to -1 cm develop around day 250. It is estimated that these negative SSH anomalies propagate southward with speed of -0.51 km/day, which is consistent with phase speeds observed in experiments Prel-E01 and Prel-E02. Along the topographic slope (Figure 21f), stronger signals larger than 1 cm are observed slightly south of 29°N starting on day 160, which correspond to timing when the anticyclone first touches the sloping topography. The southward propagation of negative SSH anomalies with phase speed of -6.35 km.day^{-1} is also seen after day 200 (black line, Figure 21f). The southward propagation associated with this feature is approximately of O(10) cm/s; one order of magnitude larger than other southward propagating signals identified on results from experiments Prel-E01, and Prel-E02. This propagation rate is consistent with advective scales of the eddy. These SSH signals along the slope are largely associated with the development of the anomalous wall-jet that was previously described (Figure 26c). Interestingly, transport anomalies observed at the Florida Straits during experiment Prel-E03 were uncorrelated with coastal SSH variability at 27°N at zero lag (black circle, Figure 20g). Similarly from results of experiments Prel-E01 and Prel-E02, transport anomalies are also strongly correlated with SSH changes at the Bahamas side at zero lag (Figure 22g). These results reinforce that changes in transport are primarily linked with changes in sea-level at the Bahamas.

6 Summary

This study aims to help improve the understanding on the FC variability. More specifically, the objective of this study is to identify the different mechanisms linking the open ocean variability associated with westward propagating signals, with the response of FC

at the western boundary. The main motivation for this study comes from the fact that westward propagating signals originating in the open North Atlantic ocean have been identified as a potential driver of a significant component (27%) of the FC variability, the transient seasonal component [*Domingues and Baringer*, 2015]. This component is defined as seasonal variability linked with variable annual phase. To accomplish this, different sets of controlled realistic high-resolution numerical experiments were proposed to address different scenarios that may arise from the interaction of westward propagating signals with the western boundary system.

In this proposal, results from three preliminary experiments (Prel-E01, Prel-E02, and Prel-E03) were analyzed to provide initial insight on the type of responses generated at the western boundary, and also to establish the baseline for future analysis performed in this study. These first three experiments were developed in the absence of the FC flow to enable an initial understanding on the responses generated by westward propagating signals impinging along the east coast of United States. While experiments Prel-E01 and Prel-E03 were initialized with single anticyclonic eddies at 27°N/71°W and 29°N/76°W, respectively, experiment Prel-E02 was initialized with a train of cyclonic and anticyclonic eddies at 27°N. Prescribed eddies had an approximate 150 km diameter, and were associated with a volume transport of $\sim$2 Sv.

Results from these preliminary experiments showed that the open ocean phase was characterized by the westward propagation of prescribed eddies at a rate controlled by the rossby wave field that developed in the wake of these eddies. Prescribed eddies also exhibited meridional motions due to conservation of potential vorticity, with a tendency of anticyclonic eddies for moving south, and of cyclonic eddies for moving north. Initial perturbations then reached the western boundary in different locations along the coast, providing an opportunity for investigating different mechanisms linked with the response generated at the Florida Straits.

The main finding reported here indicates that westward propagating signals originated in the open North Atlantic Ocean may indeed drive variability in the FC transport,

supporting the findings of *Domingues and Baringer* [2015]. Meridional transport variability at the Florida Straits generated during these preliminary experiments reached values of $\sim$0.8 Sv in experiment Prel-E02, and of $\sim$0.5 Sv and of $\sim$0.4 Sv during experiments Prel-E01 and Prel-E02, respectively. Different mechanisms have been identified in the response forced at the western boundary, such as: (i) the direct influence of the rossby wave field, and (ii) the development of wall-jets flowing along the sloping topography. Results from experiment Prel-E01 showed that the rossby wave field caused the development broad velocity anomalies in the Straits linked with transport anomalies of 0.5 Sv. Results from experiment Prel-E02 showed the development of a anomalous jet in the Florida Straits that was directly linked with the impinging anticyclonic eddy, which touched the western boundary slightly north of the Northwest Providence Channel entrance. The combination of background rossby wave effects with the anomalous jet caused stronger transport anomalies reaching values of 0.8 Sv. Results from experiment Prel-E03 showed that signals impinging in the western boundary north of the Florida Straits could still drive variability at the straits, and that the anomalous wall-jet could propagate southward along the coast, driving variability further upstream from the Florida Straits. Changes in transport are also strongly correlated with sea-level changes in the Bahamas side of the Florida Straits, which then lead changes in sea-level the Florida coast, confirming the westward propagating characteristics of the anomalies.

Another important finding from these experiments is that, even though prescribed anomalies are initially associated with well-defined time-scales due to westward propagation, non-linear processes resulting from the interaction between eddies and the rossby wave field cause the distribution of the spectral energy into different time-scales. For example, in experiment Prel-E02, the interaction of the rossby wave field with features associated directly with the eddy caused transport anomalies in a broader range of frequencies at the Florida Straits, implying small changes with periods of $\sim$100 days overlaid on larger changes with periods longer than 400 days. This is in contrast with transport anomalies observed in experiment Prel-E01, which were caused solely by the rossby wave

field, and where linked with a well-defined periodicity of $\sim$300 days.

Following these preliminary experiments, the analysis will continue with the development of additional sets of numerical experiments proposed in this study. The additional numerical experiments will help to understand different mechanisms linking the open ocean variability with changes in the FC transport. In particular, the comparison between equivalent experiments with and without the Florida Current may provide useful information on the role of the FC in modulating the response forced by impinging westward propagating signals at the western boundary region in the North Atlantic Ocean.

References

Ådlandsvik, B. (2008), Marine downscaling of a future climate scenario for the north sea, *Tellus A*, *60*(3), 451–458.

Amante, C., and B. W. Eakins (2009), *ETOPO1 1 arc-minute global relief model: procedures, data sources and analysis*, US Department of Commerce, National Oceanic and Atmospheric Administration, National Environmental Satellite, Data, and Information Service, National Geophysical Data Center, Marine Geology and Geophysics Division.

Atkinson, C., H. Bryden, J. Hirschi, and T. Kanzow (2010), On the seasonal cycles and variability of florida straits, ekman and sverdrup transports at 26 n in the atlantic ocean, *Ocean Science*, *6*(4), 837–859.

Baringer, M. O., and J. C. Larsen (2001), Sixteen years of Florida Current transport at 27 N, *Geophysical Research Letters*, *28*(16), 3179–3182.

Beal, L. M., J. M. Hummon, E. Williams, O. B. Brown, W. Baringer, and E. J. Kearns (2008), Five years of florida current structure and transport from the royal caribbean cruise ship explorer of the seas, *Journal of Geophysical Research: Oceans (1978–2012)*, *113*(C6).

Beckman, A., and D. Haidvogel (1993), Numerical simulation of flow around a tall isolated seamount, *J. Phys. Oceanogr*, *23*, 1736–1753.

Berloff, P., I. Kamenkovich, and J. Pedlosky (2009), A mechanism of formation of multiple zonal jets in the oceans, *Journal of Fluid Mechanics*, *628*, 395–425.

Blaas, M., C. Dong, P. Marchesiello, J. C. McWilliams, and K. D. Stolzenbach (2007), Sediment-transport modeling on southern californian shelves: A roms case study, *Continental shelf research*, *27*(6), 832–853.

Böning, C. W., and R. G. Budich (1991), Seasonal transport variation in the western subtropical north-atlantic: Eperiments with an eddy-resolving model, *Journal of Physical Oceanography*, *21*, 1271–1289.

Bryden, H. L., W. E. Johns, and P. M. Saunders (2005), Deep western boundary current east of abaco: Mean structure and transport, *Journal of Marine Research*, *63*, 35–57.

Byrne, D. A., A. L. Gordon, and W. F. Haxby (1995), Agulhas eddies: A synoptic view using geosat erm data, *Journal of Physical Oceanography*, *25*(5), 902–917.

Calado, L., A. Gangopadhyay, and I. Silveira (2008), Feature-oriented regional modeling and simulations (FORMS) for the western South Atlantic: Southeastern Brazil region, *Ocean Modelling*, *25*(1-2), 48–64.

Chelton, D. B., and M. G. Schlax (1996), Global observations of oceanic rossby waves, *Science*, pp. 234–243.

Czeschel, L., C. Eden, and R. J. Greatbatch (2012), On the driving mechanism of the annual cycle of the Florida Current transport, *Journal of Physical Oceanography*, *42*(5), 824–839.

Domingues, R., and M. Baringer (2015), Remote forcing of the Florida Current on Seasonal Time-scales, *to be submitted to Geophysical Research Letters*.

Elipot, S., C. Hughes, S. Olhede, and J. Toole (2013), Coherence of western boundary pressure at the rapid wave array: boundary wave adjustments or deep western boundary current advection?, *Journal of Physical Oceanography*, *43*(4), 744–765.

Ezer, T. (2013), Sea level rise, spatially uneven and temporally unsteady: Why the us east coast, the global tide gauge record, and the global altimeter data show different trends, *Geophysical Research Letters*, *40*(20), 5439–5444.

Ezer, T., and L. P. Atkinson (2014), Accelerated flooding along the us east coast: on the impact of sea-level rise, tides, storms, the gulf stream, and the north atlantic oscillations, *Earth's Future*, *2*(8), 362–382.

Fox, D., M. Carnes, and J. Mitchell (1992), Characterizing major frontal systems: A nowcast/forecast system for the Northwest Atlantic, *Oceanography*, *5*(1), 49–53.

Frajka-Williams, E., W. Johns, C. Meinen, L. Beal, and S. Cunningham (2013), Eddy impacts on the Florida Current, *Geophysical Research Letters*, *40*(2), 349–353.

Guinehut, S., P.-Y. Le Traon, and G. Larnicol (2006), What can we learn from Global Altimetry/Hydrography comparisons?, *Geophysical Research Letters*, *33*(10).

Halliwell Jr, G. R., P. Cornillon, and D. A. Byrne (1991), Westward-propagating sst anomaly features in the sargasso sea, 1982-88, *Journal of physical oceanography*, *21*(5), 635–649.

Haney, R. L. (1991), On the pressure gradient force over steep topography in sigma coordinate ocean models, *Journal of Physical Oceanography*, *21*(4), 610–619.

Johns, W., L. Beal, M. Baringer, J. Molina, S. Cunningham, T. Kanzow, and D. Rayner (2008), Variability of shallow and deep western boundary currents off the bahamas during 2004-05: Results from the 26 n rapid-moc array, *Journal of Physical Oceanography*, *38*(3), 605–623.

Johns, W. E., T. L. Townsend, D. M. Fratantoni, and W. D. Wilson (2002), On the atlantic inflow to the caribbean sea, *Deep Sea Research Part I: Oceanographic Research Papers*, *49*(2), 211–243.

Kanzow, T., H. Johnson, D. Marshall, S. Cunningham, J.-M. Hirschi, A. Mujahid, H. Bryden, and W. Johns (2009), Basinwide integrated volume transports in an eddy-filled ocean, *Journal of Physical Oceanography*, *39*(12), 3091–3110.

Killworth, P. D., D. B. Chelton, and R. A. de Szoeke (1997), The speed of observed and theoretical long extratropical planetary waves, *Journal of Physical Oceanography*, *27*(9), 1946–1966.

Large, W. G., J. C. McWilliams, and S. C. Doney (1994), Oceanic vertical mixing: A review and a model with a nonlocal boundary layer parameterization, *Reviews of Geophysics*, *32*(4), 363–403.

Larsen, J. (1992), Transport and heat flux of the Florida current at 27 degrees N derived from cross-stream voltages and profiling data: Theory and observations, *Philosophical Transactions of the Royal Society of London. Series A: Physical and Engineering Sciences*, *338*(1650), 169–236.

Leaman, K. D., and R. L. Molinari (1987a), Topographic modification of the Florida Current by Little Bahama and Great Bahama Banks, *Journal of physical oceanography*, *17*(10), 1724–1736.

Leaman, K. D., R. L. Molinari, and P. S. Vertes (1987b), Structure and variability of the florida current at 27 n: April 1982-july 1984, *Journal of Physical Oceanography*, *17*(5), 565–583.

Lee, T. N., W. Johns, R. Zantopp, and F. Schott (1990), Western boundary current structure and variability east of abaco, bahamas at 26.5 n, *Journal of Physical Oceanography*, *20*(3), 446–466.

Lee, T. N., W. E. Johns, R. J. Zantopp, and E. R. Fillenbaum (1996), Moored observations of western boundary current variability and thermohaline circulation at 26.5 in the subtropical north atlantic, *Journal of Physical Oceanography*, *26*(6), 962–983.

Locarnini, R., et al. (2013), World Ocean Atlas 2013. Vol. 1: Temperature, *A. Mishonov, Technical Ed. NOAA Atlas NESDIS*, *73*, 40.

Meinen, C. S., M. O. Baringer, and R. F. Garcia (2010), Florida Current transport variability: An analysis of annual and longer-period signals, *Deep Sea Research Part I: Oceanographic Research Papers*, *57*(7), 835–846.

Milliff, R. F., and J. C. McWilliams (1994), The evolution of boundary pressure in ocean basins, *Journal of physical oceanography*, *24*(6), 1317–1338.

Molinari, R. L., E. Johns, and J. F. Festa (1990), The annual cycle of meridional heat flux in the atlantic ocean at 26.5 n, *Journal of Physical Oceanography*, *20*(3), 476–482.

Niiler, P. P., and W. S. Richards (1973), Seasonal variability of florida current, *Journal of Marine Research*, *31*(3), 144–167.

Nof, D. (1988), Eddy-wall interactions, *Journal of Marine Research*, *46*(3), 527–555.

Nof, D. (1999), Strange encounters of eddies with walls, *Journal of Marine Research*, *57*(5), 739–761.

Oliveira, F. S., and P. S. Polito (2013), Characterization of westward propagating signals in the South Atlantic from altimeter and radiometer records, *Remote Sensing of Environment*, *134*, 367–376.

Olson, D. B., F. A. Schott, R. J. Zantopp, and K. D. Leaman (1984), The mean circulation east of the bahamas as determined from a recent measurement program and historical xbt data, *Journal of Physical Oceanography*, *14*(9), 1470–1487.

Polito, P. S., and W. T. Liu (2003), Global characterization of Rossby waves at several spectral bands, *Journal of Geophysical Research: Oceans (1978–2012)*, *108*(C1).

Robinson, A., M. Spall, and N. Pinardi (1988), Gulf Stream simulations and the dynamics of ring and meander processes, *J. Phys. Oceanogr*, *18*(12), 1811–1854.

Rousset, C., and L. M. Beal (2011), On the seasonal variability of the currents in the Straits of Florida and Yucatan Channel, *Journal of Geophysical Research: Oceans (1978–2012)*, *116*(C8).

Schott, F. A., T. N. Lee, and R. Zantopp (1988), Variability of structure and transport of the Florida Current in the period range of days to seasonal, *Journal of Physical Oceanography*, *18*(9), 1209–1230.

Shchepetkin, A., and J. C. McWilliams (2000), A family of finite-volume methods for computing pressure gradient force in an ocean model with a topography-following vertical coordinate, *Preprint*.

Shchepetkin, A. F., and J. C. McWilliams (2005), The regional oceanic modeling system (roms): a split-explicit, free-surface, topography-following-coordinate oceanic model, *Ocean Modelling*, *9*(4), 347–404.

Sheinbaum, J., J. Candela, A. Badan, and J. Ochoa (2002), Flow structure and transport in the yucatan channel, *Geophysical Research Letters*, *29*(3), 10–1.

Simmons, H. L., and D. Nof (2002), The squeezing of eddies through gaps, *Journal of physical oceanography*, *32*(1), 314–335.

Stommel, H. (1948), The theory of the electric field induced in deep ocean currents, *J. Mar. Res*, *7*(3), 386–392.

Stommel, H. M. (1958), *The Gulf Stream: a physical and dynamical description*, Univ of California Press.

Zweng, M., et al. (2013), World ocean atlas 2013, Volume 2: Salinity, *A. Mishonov, Technical Ed. NOAA Atlas NESDIS*.

Table 1: Parameters defining configuration of vertical layers on the grid used in this study.

Parameter	Value	Description
N	30	Number of vertical layers
Vtransform	2	Transformation equation
Vstretching	4	Vertical stretching function
Theta_s	4	Surface stretching parameter
Theta_b	0	Bottom stretching parameter
Tcline	10	Critical depth [m]

Table 2: Set of experiments proposed in this study.

Experiment	Relatioship to Questions	Description
Cntr-E01	N/A	Control run initialized with flat isopycnals, no FC, and no eddies
Prel-E01	Q1	Preliminary experiment initialized with no FC, and single anticyclone at 27°N, 70.5°W
Prel-E02	Q1	Preliminary experiment initialized with no FC, and train of eddies along 27°N
Prel-E03	Q1	Preliminary experiment initialized with no FC, and single anticyclone at 29°N, 76°W
ARCR-E0x	Q3, Q2, Q4	Set of experiments initialized with no FC, and single anticyclonic or cyclonic eddies in different latitudes
EdFul-E0x	Q5, Q7	Set of experiments initialized with no FC, and train of eddies in different latitudes
Cntr-E02	N/A	Control run initialized with background flow from the FC, and no eddies in the interior
ModFC-E0x	Q6	Set of experiments initialized with the FC, and with eddies prescribed in the interior
LTerm-E0x	Q7	Set of experiments initialized with the FC, and with constant inflow of eddies through the boundary

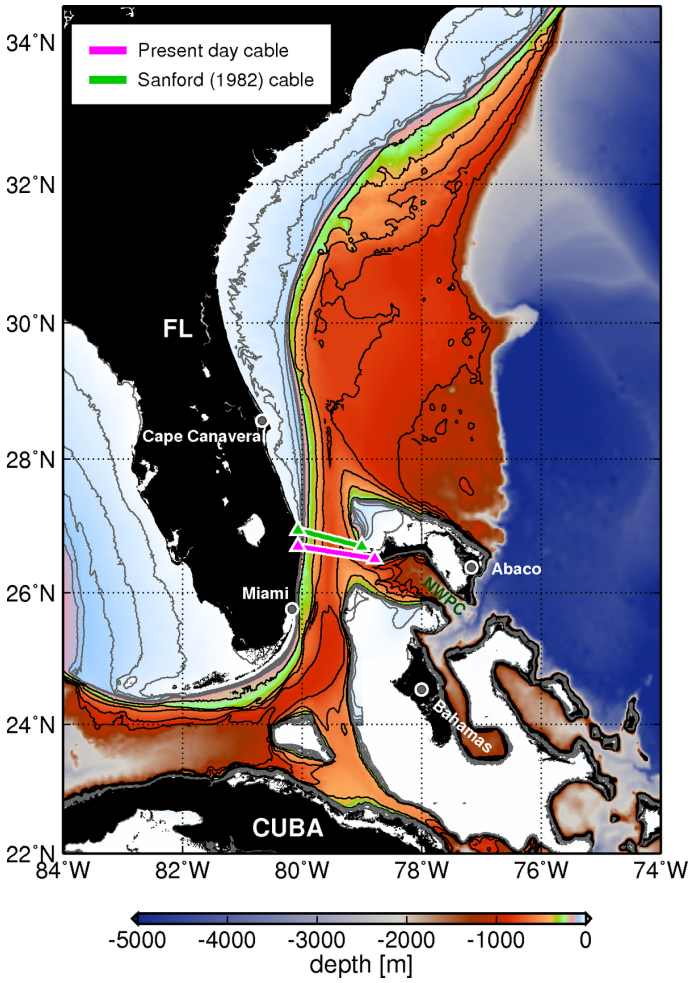

Figure 1: Location of the Florida straits. Highlighted are the locations of the telefone cables used to estimate the Florida Current volume transport, and the location of relevant landmarks in the region of study, such as the Northwest Providence Channel (NWPC). Thin black lines show bathymetric contours every 200 m for depths between 100 m and 1000 m, while thin gray lines show bathymetric contours every 20 m for depths shallower than 100 m.

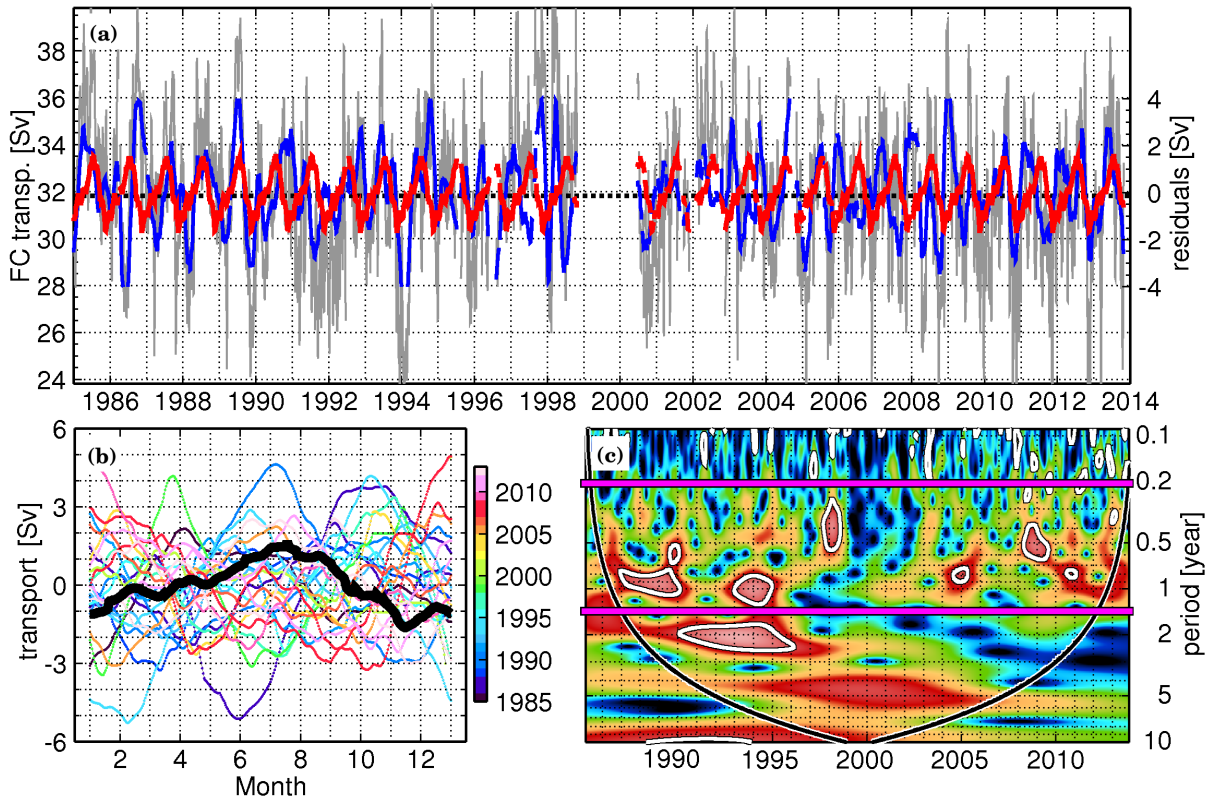

Figure 2: (a) Florida Current transport time-series (raw, light gray line) derived from measurements of voltage differences accross the straits of Florida using telephone cables. Overlaid is the climatological annual cycle for the Florida Current during 1985-2013 (red line) and the transient component (blue line). (b) Seasonal variability of the Florida Current transport during 1985-2013. (c) Wavelet transform for the Florida Current transport. The thick white lines highlight peaks in the spectral power that are significant at the 95% confidence level, while the black line marks the cone of influence for the analysis. The magenta lines delimits the 73-525 days frequency band.

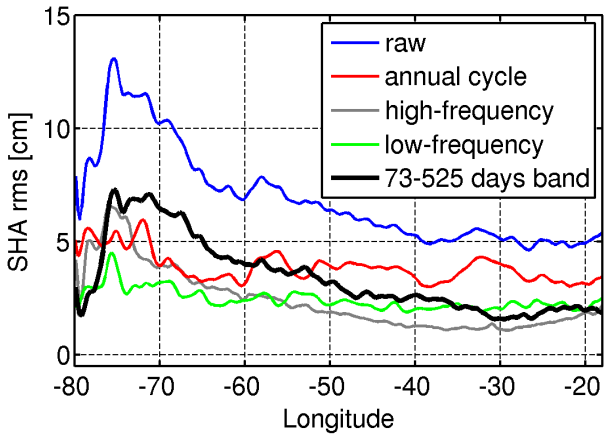

Figure 3: SHA Root Mean Square along 27°N based on: raw (blue line), annual cycle (red line), high-frequency component (< 73 days, gray line), low-frequency component(> 525 days, green line), 73-525 days frequency band (blue line).

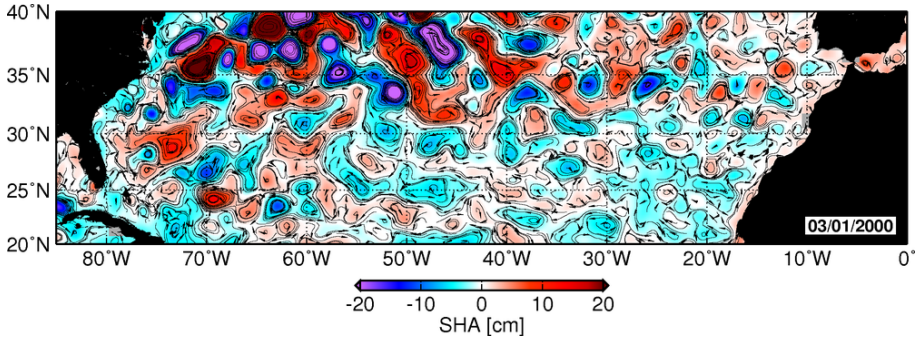

Figure 4: SHA field for March 1st, 2000, filtered at the 73-525 days frequency band. Overlaid is the SHA-derived surface geostrophic velocity vectors.

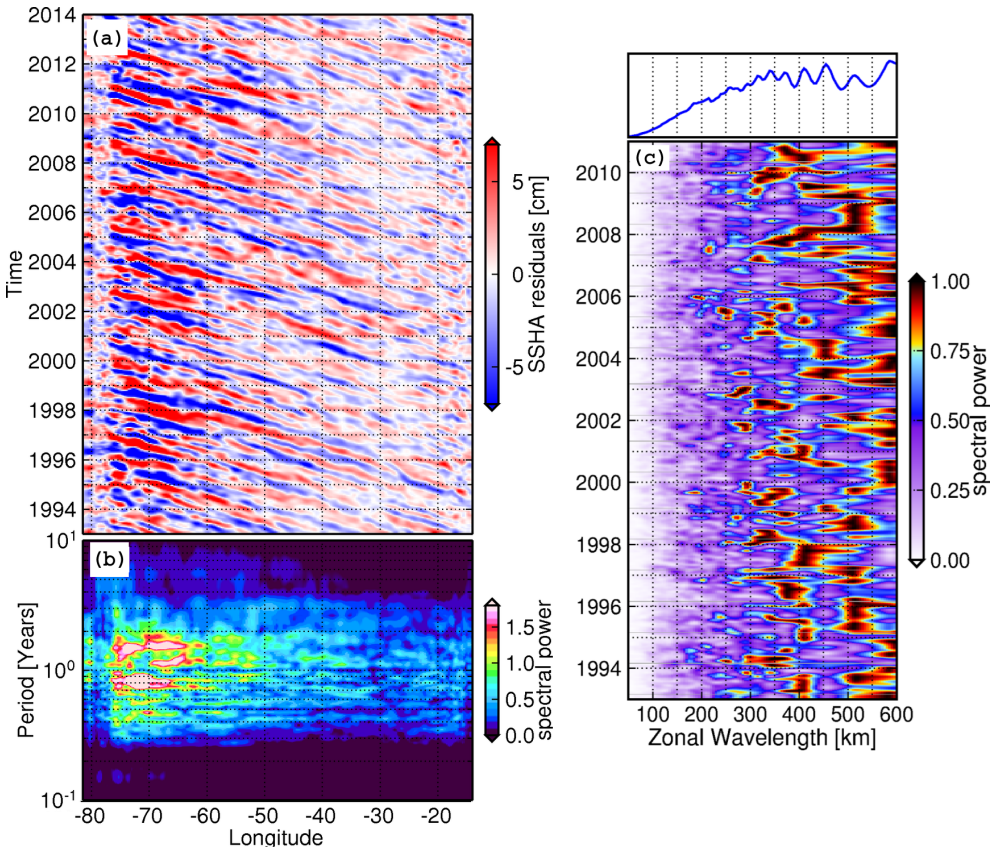

Figure 5: (a) SHAr hovmoller (longitude-time) diagram along 27°N. (b) Normalized power spectrum density from SHAs along 27°N for each longitude. (c) Wavelengths associated with SHAr along 27°N estimated using a fast-fourier transform.

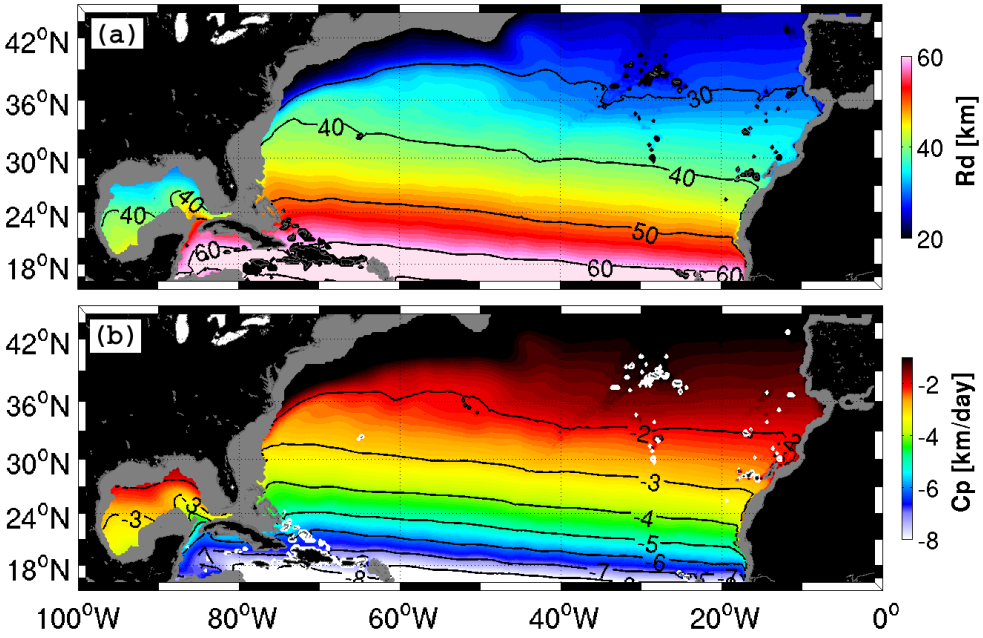

Figure 6: (a) Internal radius of deformation based on climatological conditions the Word Ocean Atlas 2013 calculated using Equations . (b) westward propagating phases speeds for long, linear, first-baroclinic Rossby waves.

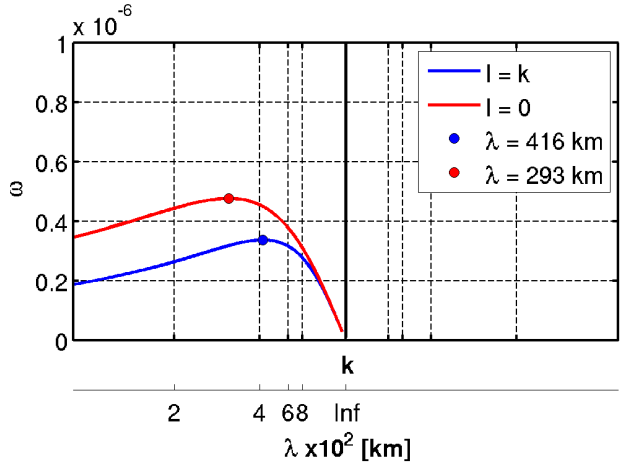

Figure 7: Dispersion relationship for first mode baroclinic rossby waves setting Rd equal to 47 km at 27°N, and using equal zonal and meridional wavenumbers (k=l, blue line), and also setting setting the meridional wavenumber to zero (l=0, red line).

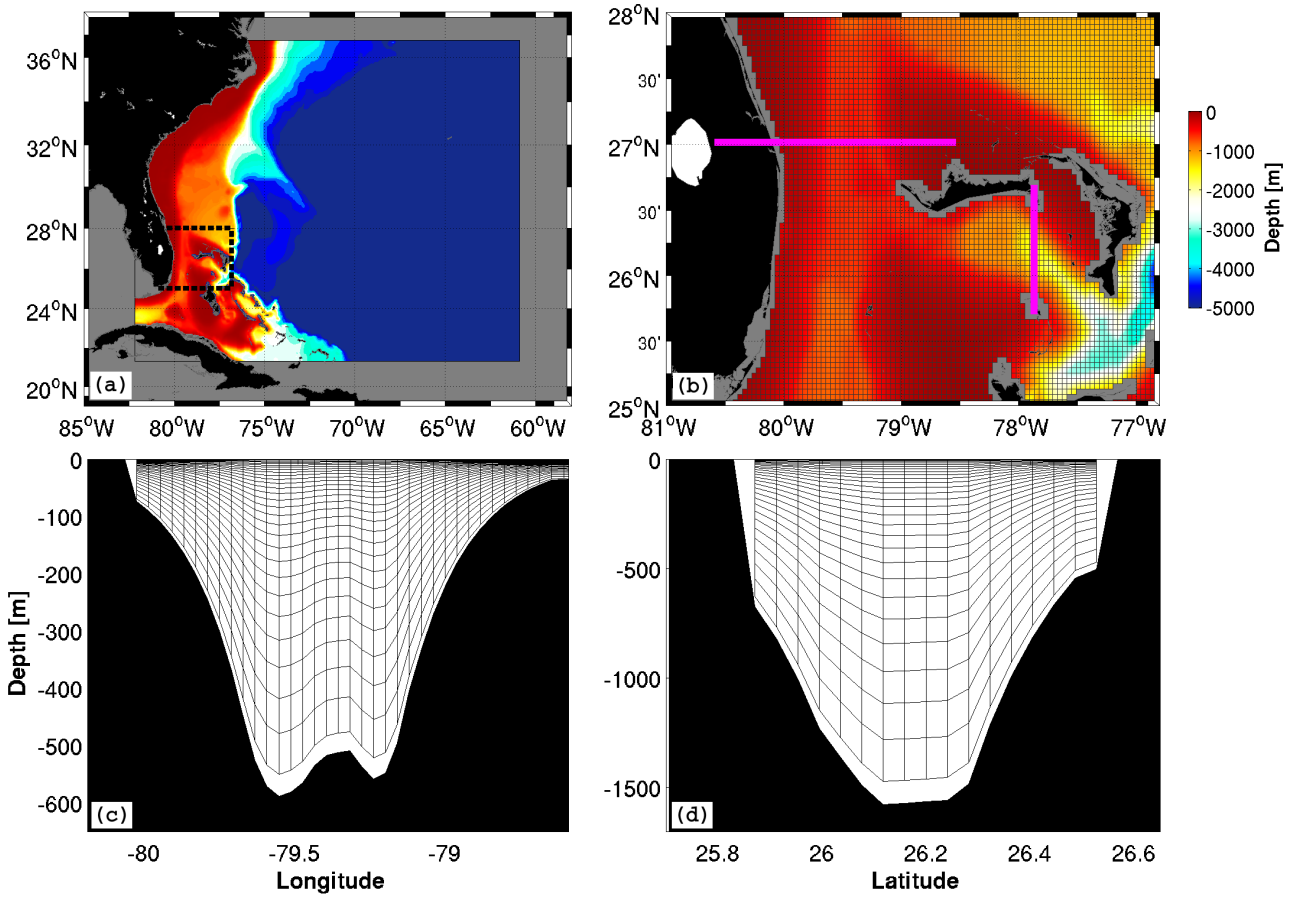

Figure 8: (a) Model domain used for numerical experiments developed in this study using ROMS. The grid has an horizontal resolution of aproximately $^{1/25}$degree with 540 X 390 points. (b) Grid configurations shown in detail at the Florida Straits. The magenta lines show the location of sections across (c) the Florida Straits, and (d) the Northwest Providence Channel, showing the configuration of vertical layers at these locations.

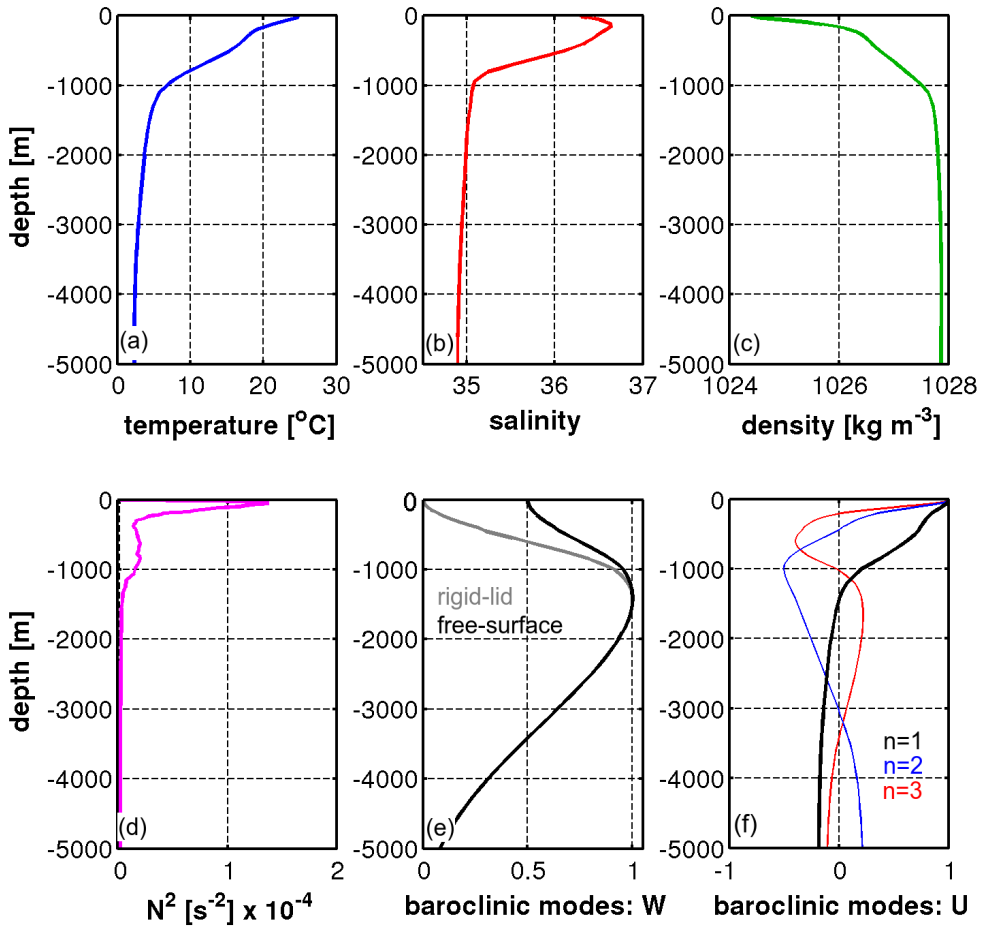

Figure 9: (a) Temperture, (b) salinity, and (c) density profiles used as background conditions for model initialization, and its derived (d) buoyancy frequency. Baroclinic modes linked with the (e) vertical velocity and density structure, and with the (f) horizontal velocity and pressure field. Modes are solved using a rigid-lid boundary condition. In panel (e), the modified first baroclinic mode for vertical velocity ($\phi_{1_m}(z)$) is shown as the thick black line.

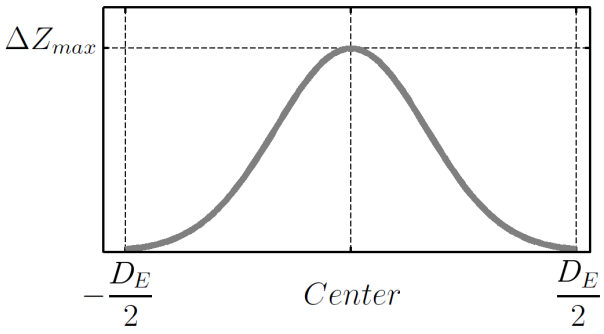

Figure 10: Gaussian function used to apply vertical displacements on isopycnal surfaces, where D_E is the radius of the eddy, and ΔZ_{max} is the maximum vertical displacement allowed.

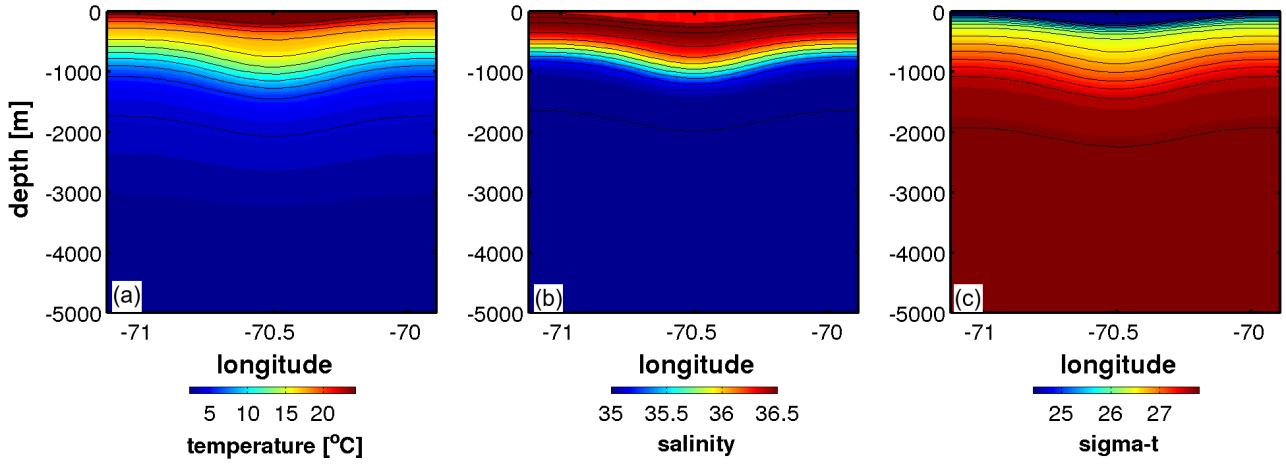

Figure 11: (a) Temperature, (b) salinity, and (c) density structure of an anticyclonic feature used as initial conditions for experiment Prel-E01.

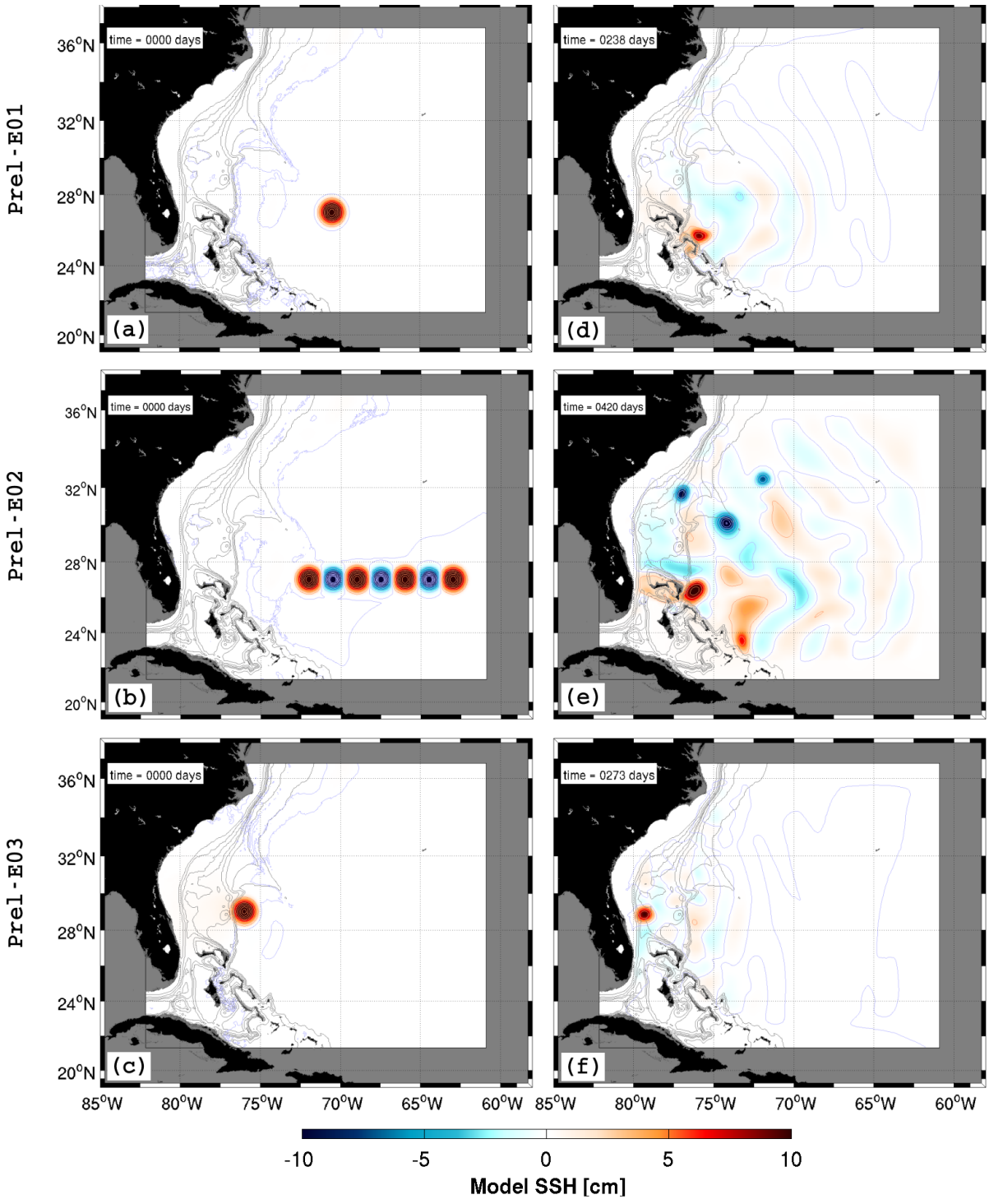

Figure 12: SSH signature during initialization (left column) and during interaction with the western boundary (right column) for experiments Prel-E01, Prel-E02, and Prel-E03.

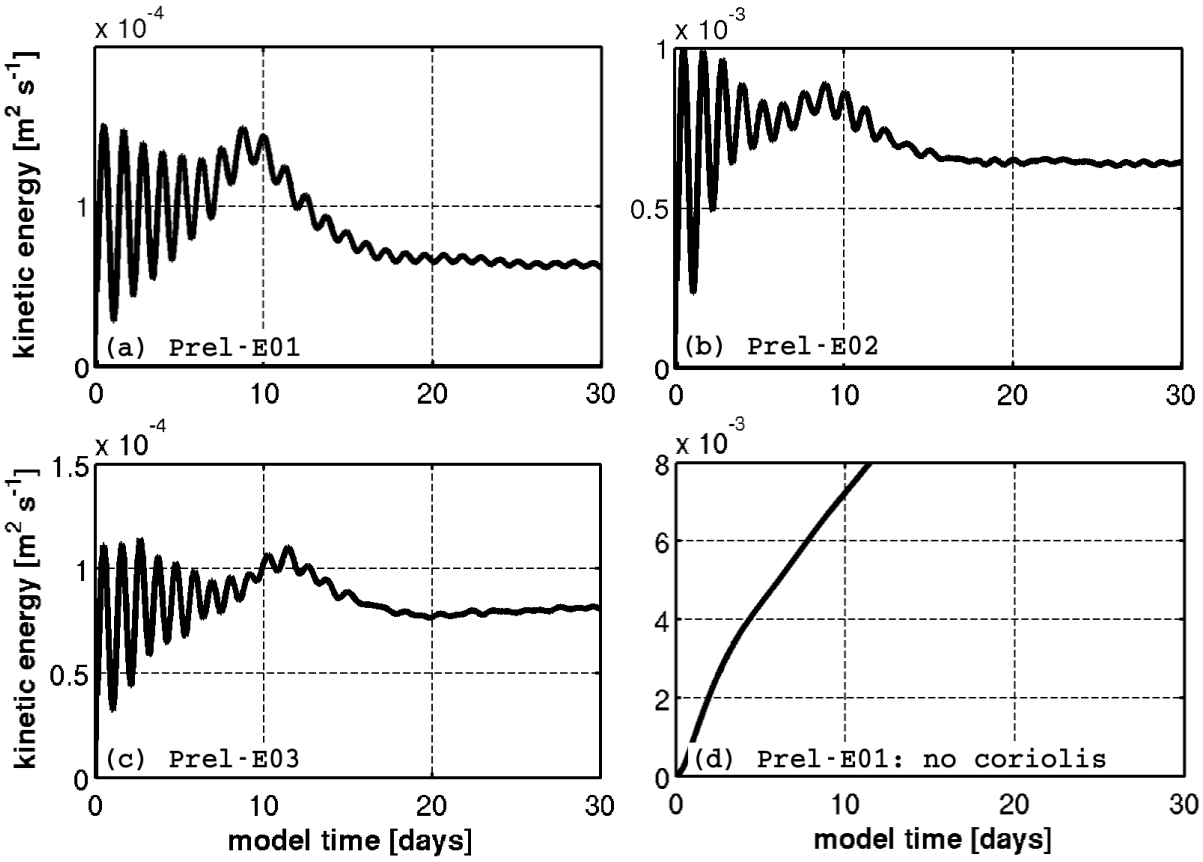

Figure 13: Temporal evolution of domain averaged kinetic energy during model spin-up on diagnostic mode for experiments (a) Prel-E01 and (b) Prel-E02.

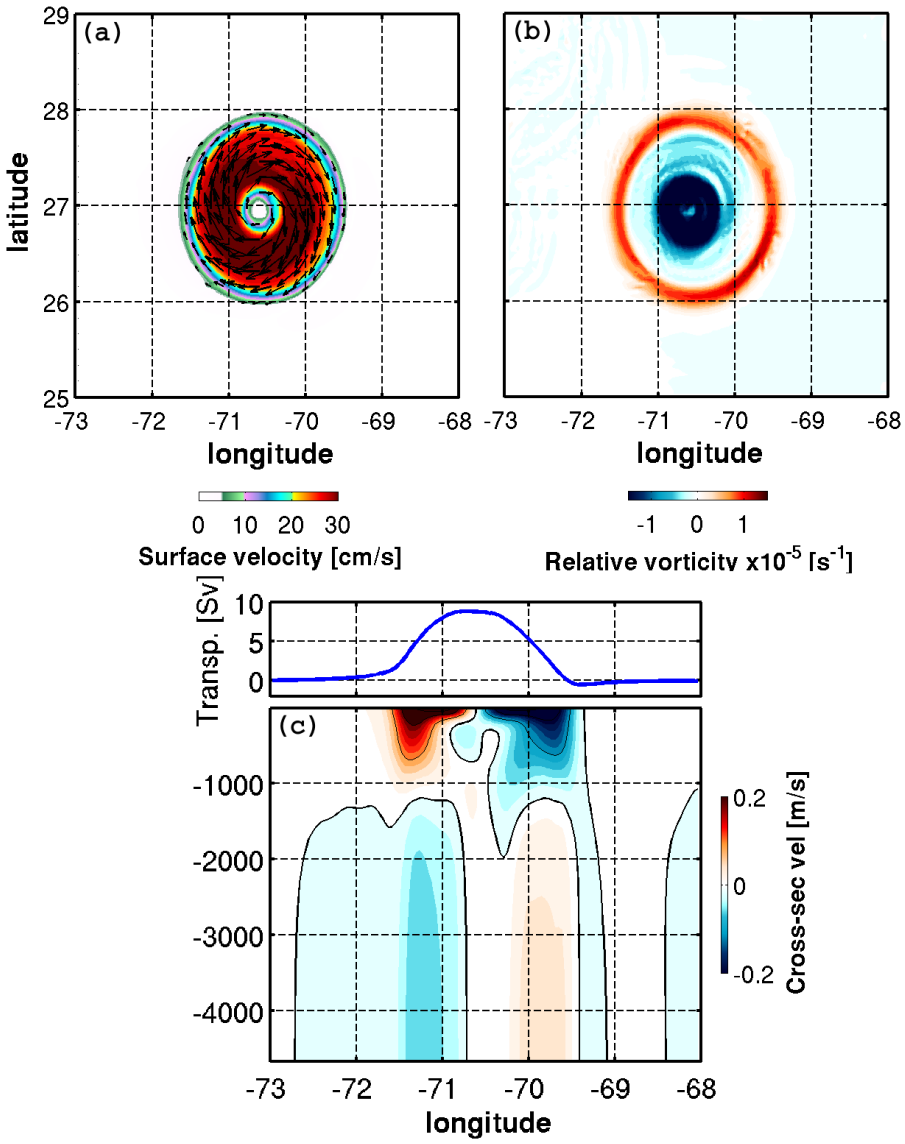

Figure 14: (a) Surface velocity field, (b) surface relative vorticity field, and (c) vertical velocity structure of the eddy after full adjustment during spin up phase on diagnostic mode for experiment Prel-E01.

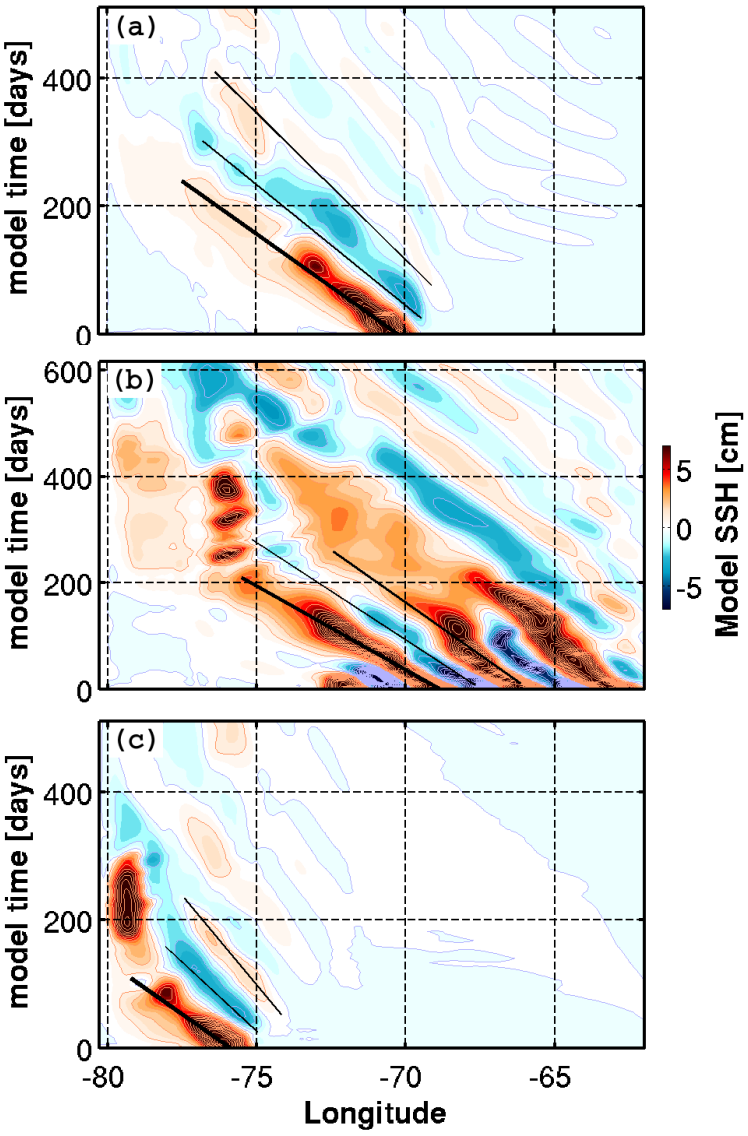

Figure 15: Hovmoller (longitude-time) diagrams of SSH along 27°N for experiments (a) Prel-E01, and (b) Prel-E02, and along 29°N for experiment (c) Prel-E03. Black lines indicate westward phase propagation.

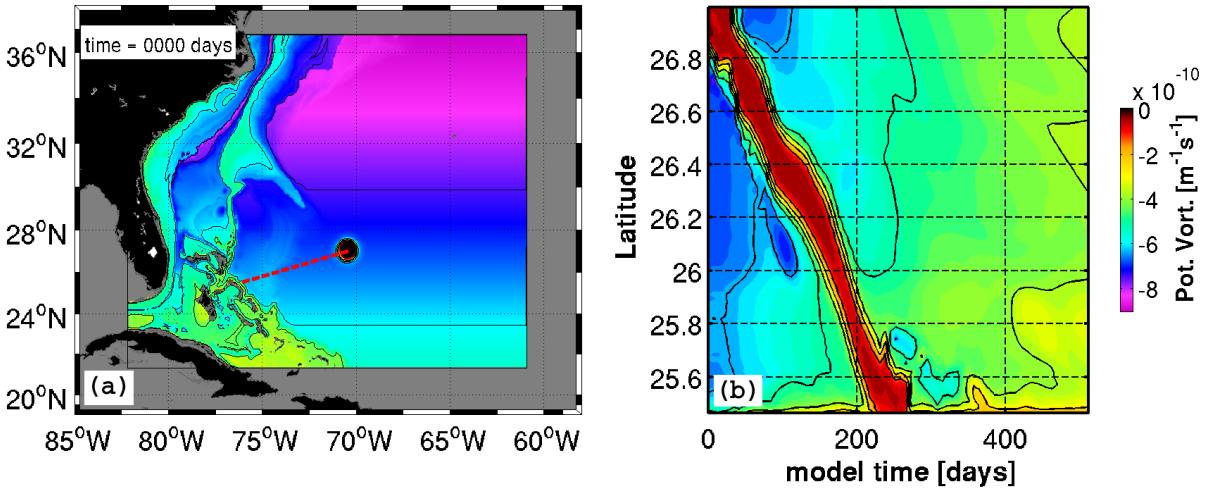

Figure 16: (a) Potential vorticity field for experiment Prel-E01 during model initialization. Red dashed-line indicates the path taken by the anticyclonic eddy during model time integration. (b) Time-latitude hovmoller diagram of potential vorticity field along the path taken by the anticyclonic eddy.

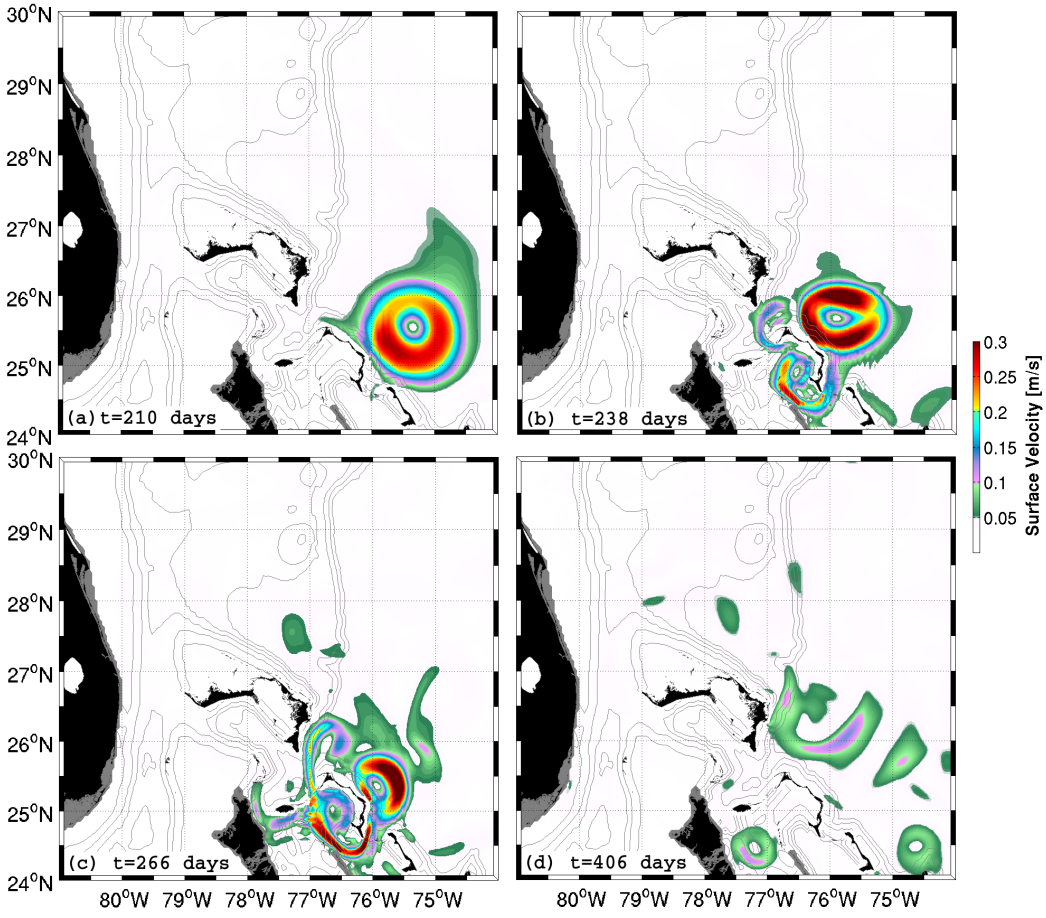

Figure 17: Surface velocity in the proximity and at the Florida Straits for experiment Prel-E01 at: (a) day 210, (b) day 238, (c) day 266, and (d) day 406.

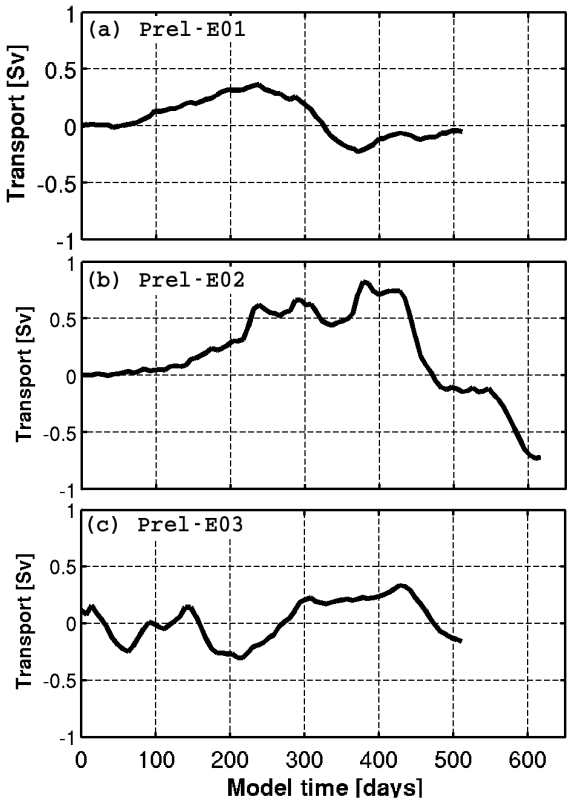

Figure 18: Time-series of volume transport anomalies across the Florida Straits (26.8°N) from experiments (a) Prel-E01, and (b) Prel-E02.

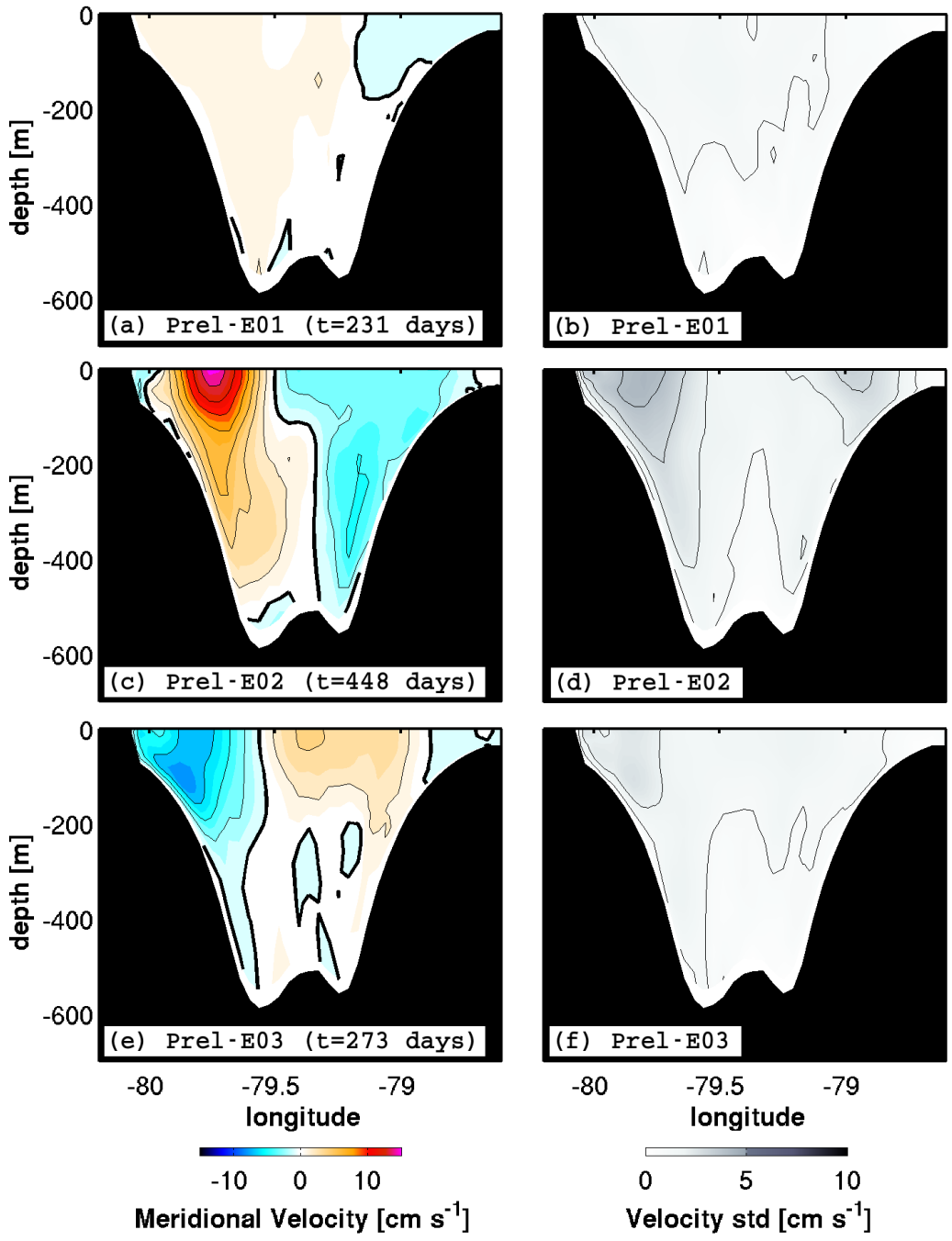

Figure 19: Cross-section velocity at the Florida Straits for experiment: (a) Prel-E01 at 210 days; (c) Prel-E02 at 448 days; and (e) Prel-E03 at day 273. Standard deviation associated with cross-section velocity variability generated at the Florida Straits for experiments (b) Prel-E01, (d) Prel-E02, and (e) Prel-E03.

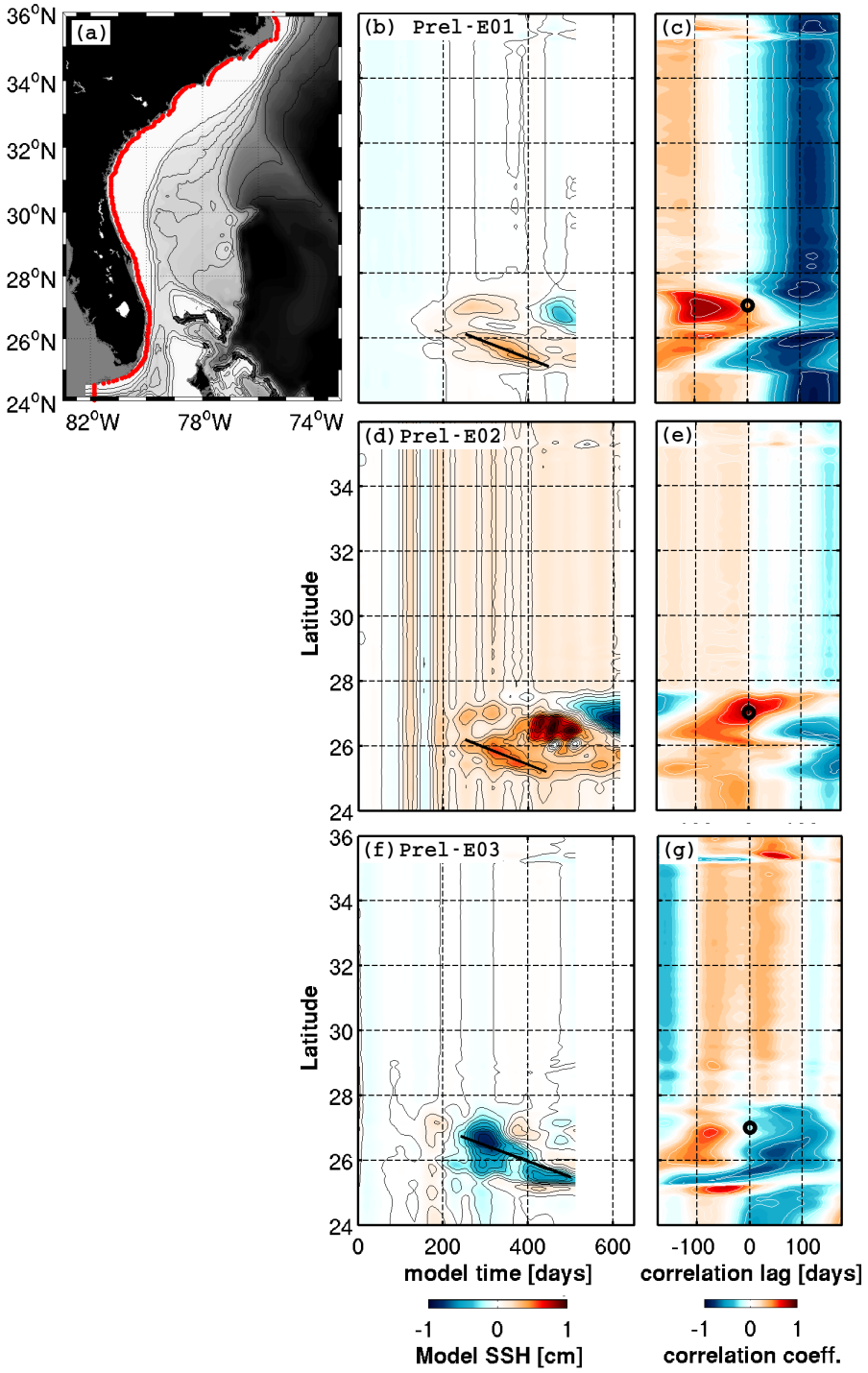

Figure 20: (a) Location of coastal SSH time-series retrieved from modeling outputs. (b) Latitude-time hovmoller diagram of coastal SSH for experiment Prel-E01. (c) Correlation coefficients between coastal SSH and meridional transport at the Florida Straits plotted as a function of correlation lag (abscissa) and latitude (ordinate). The location of the Florida Straits (27°N) is highlighted as black circle at zero lag. Panels (d) and (e) exhibit similar results for experiment Prel-E02, and (f) and (g) for experiment Prel-E03. Contours in SSH

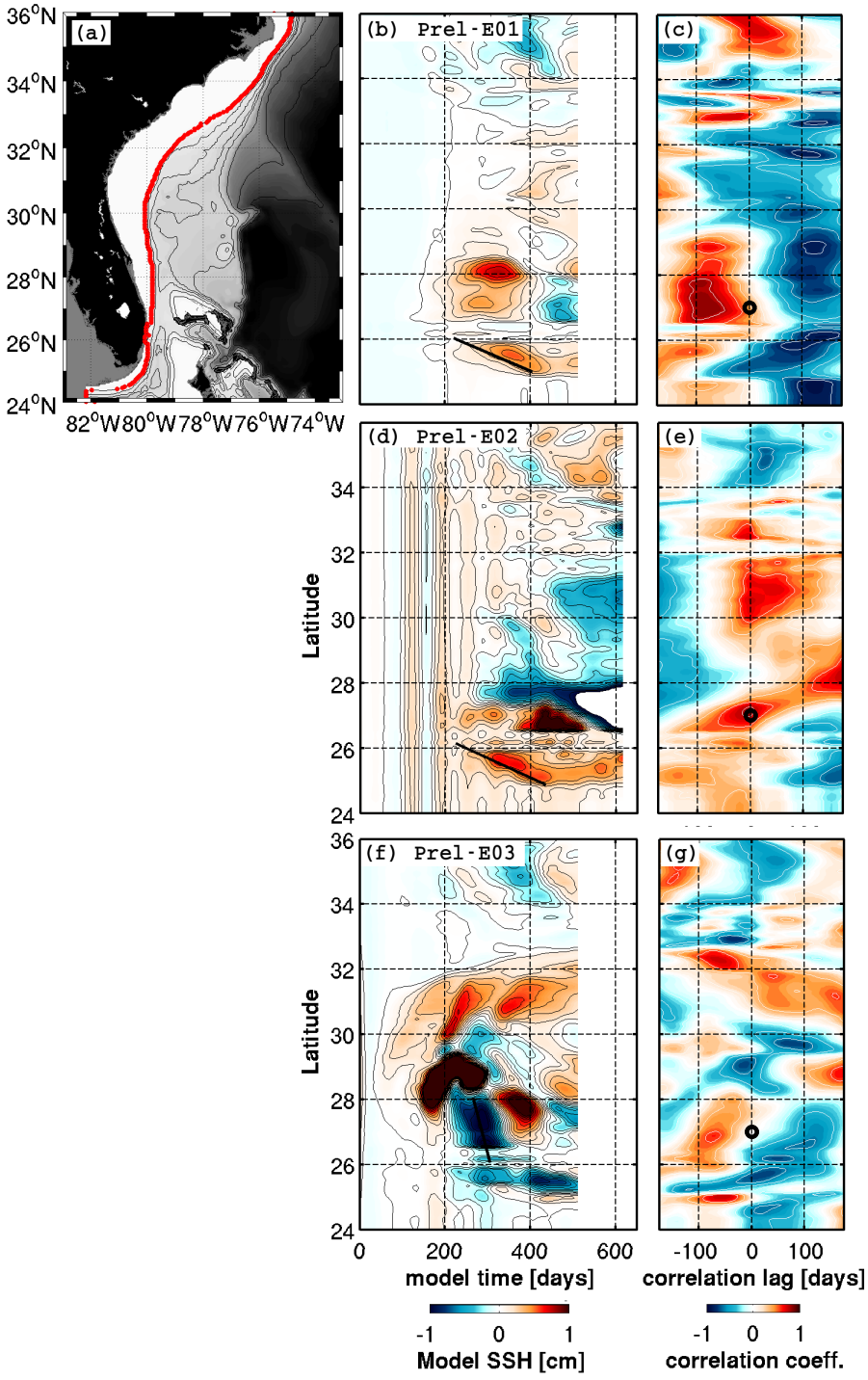

Figure 21: Same as Figure 20, but for SSH time-series retrieved along the shelf break (a).

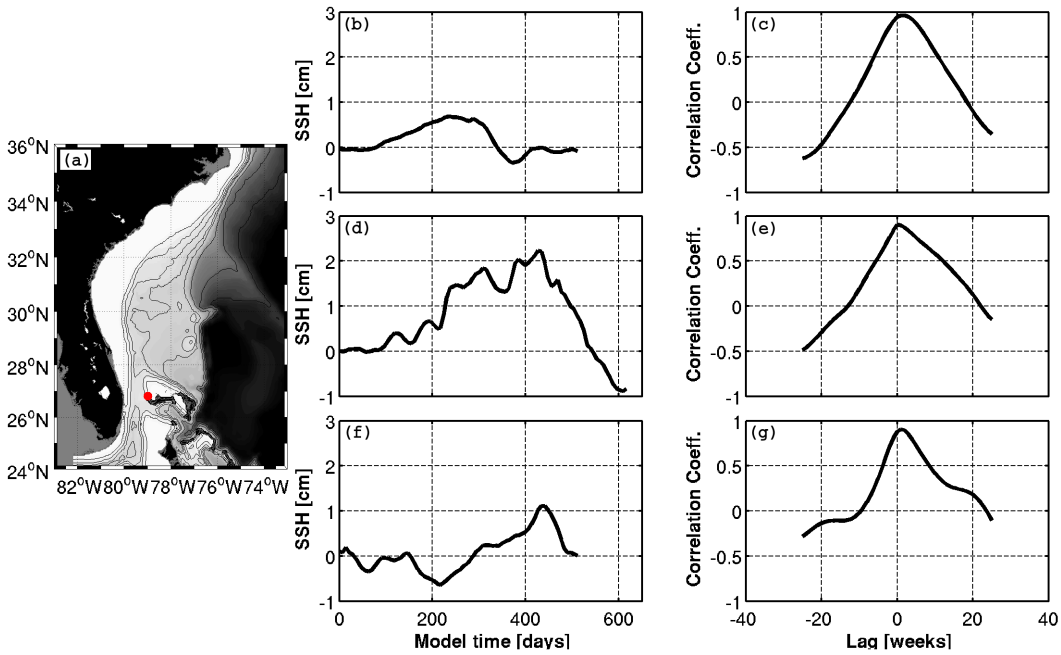

Figure 22: (a) Location where SSH time-series were retrieved at the Bahamas for numerical experiments performed in this study. SSH time-series at the Bahamas for experiments (b) Prel-E01, (d) Prel-E02, and (f) Prel-E03. Lagged correlation analysis between bahamas SSH and meridional transport at the Florida Straits based on modeling outputs from experiments (c) Prel-E01, (e) Prel-E02, and (g) Prel-E03.

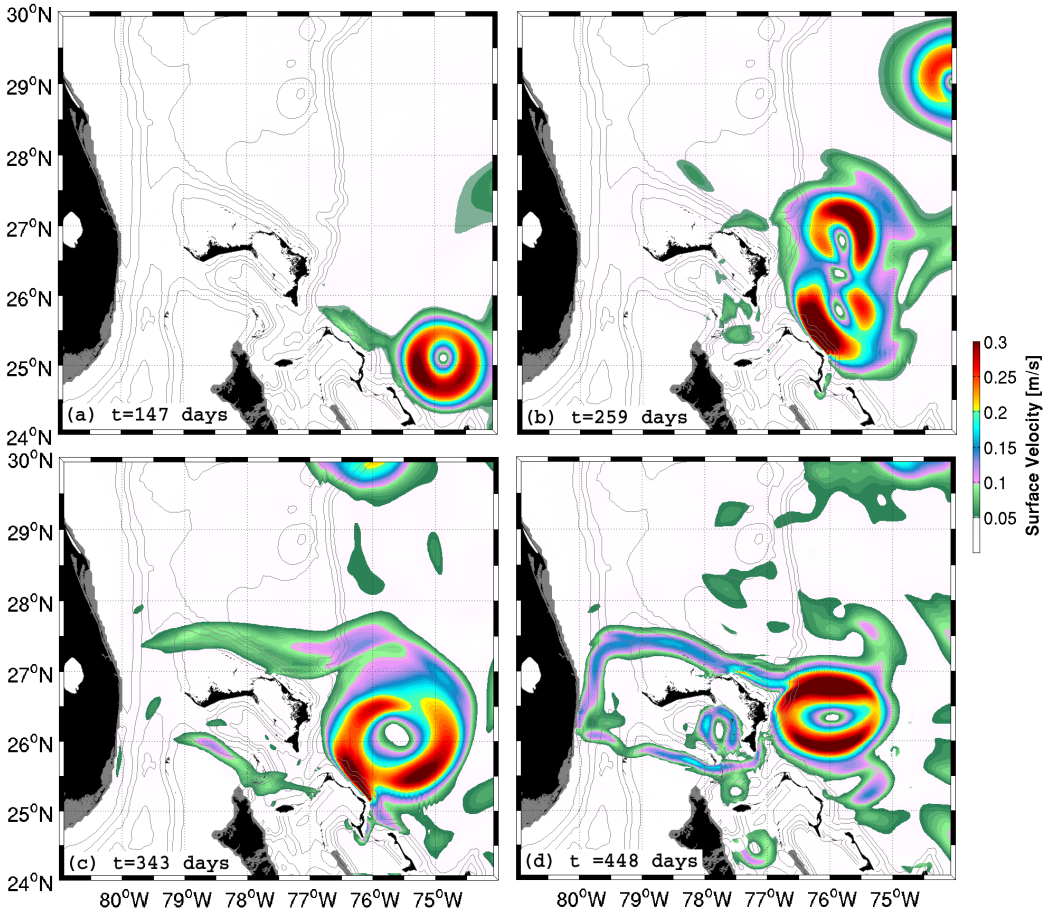

Figure 23: Surface velocity in the proximity and at the Florida Straits for experiment Prel-E02 at: (a) day 147, (b) day 259, (c) day 343, and (d) day 448.

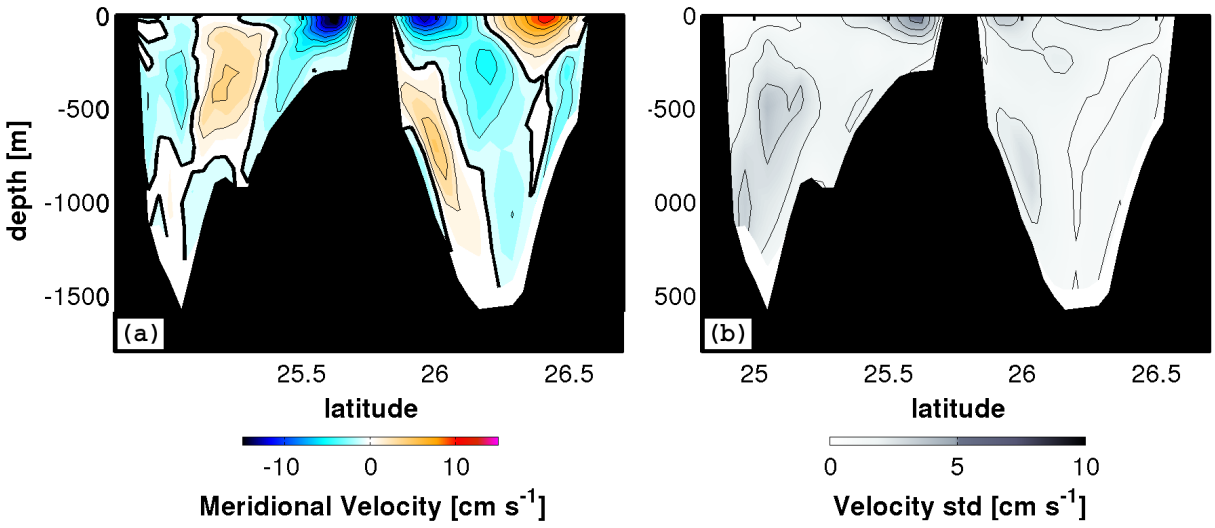

Figure 24: (a) Cross-section velocity at the Northwest Providence Channel for experiment Prel-E02 at 441 days. (b) Standard deviation associated with velocity variability at the Northwest Providence Channel.

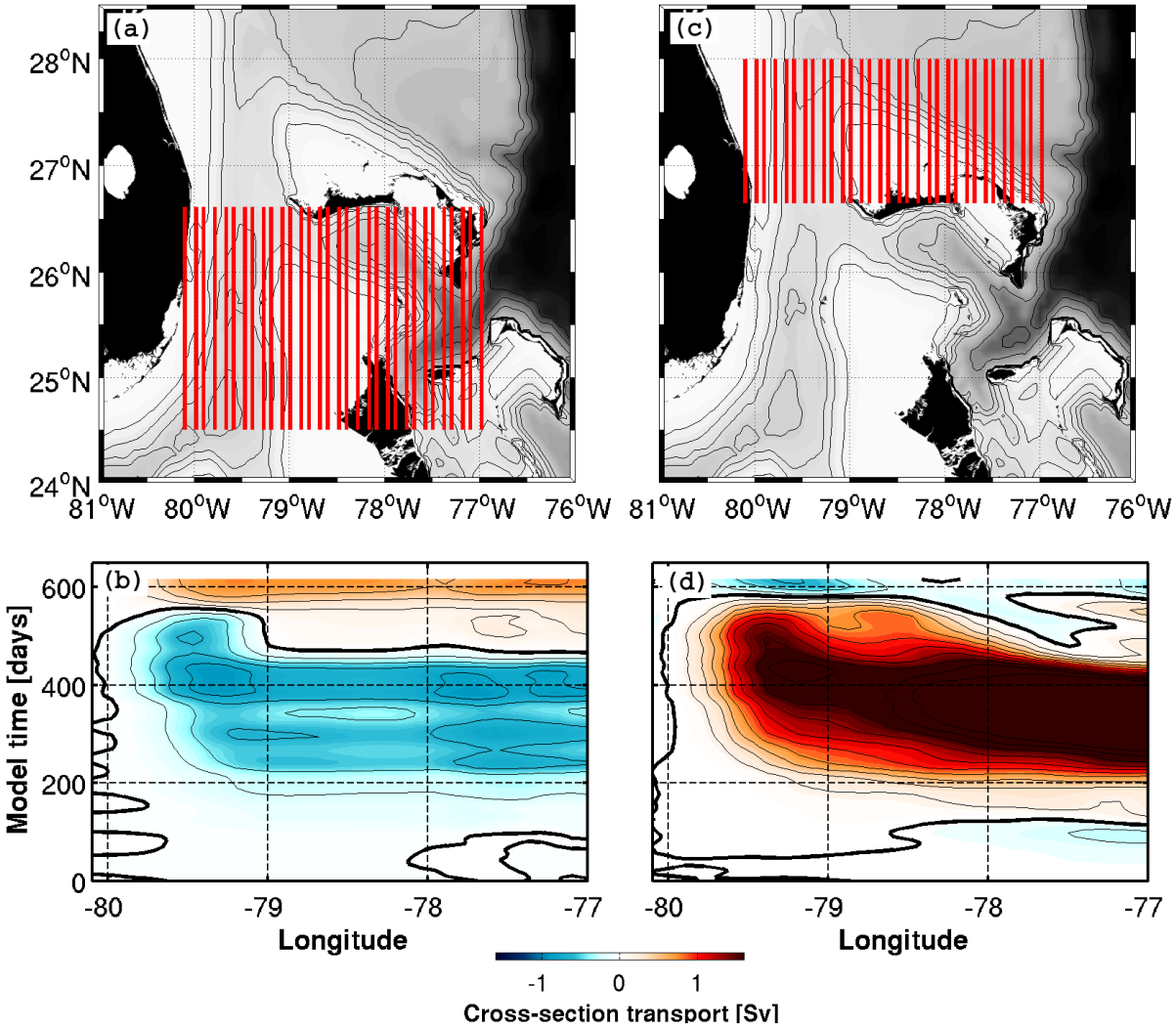

Figure 25: (a) Location of meridional sections (red lines) at the Northwest Providence Channel, where the evolution of zonal cross-section transport for experiment Prel-E02 is evaluated and ploted in (b). Panels (c) and (d) are same as (a) and (b), respectively, but for the region north of the Bahamas.

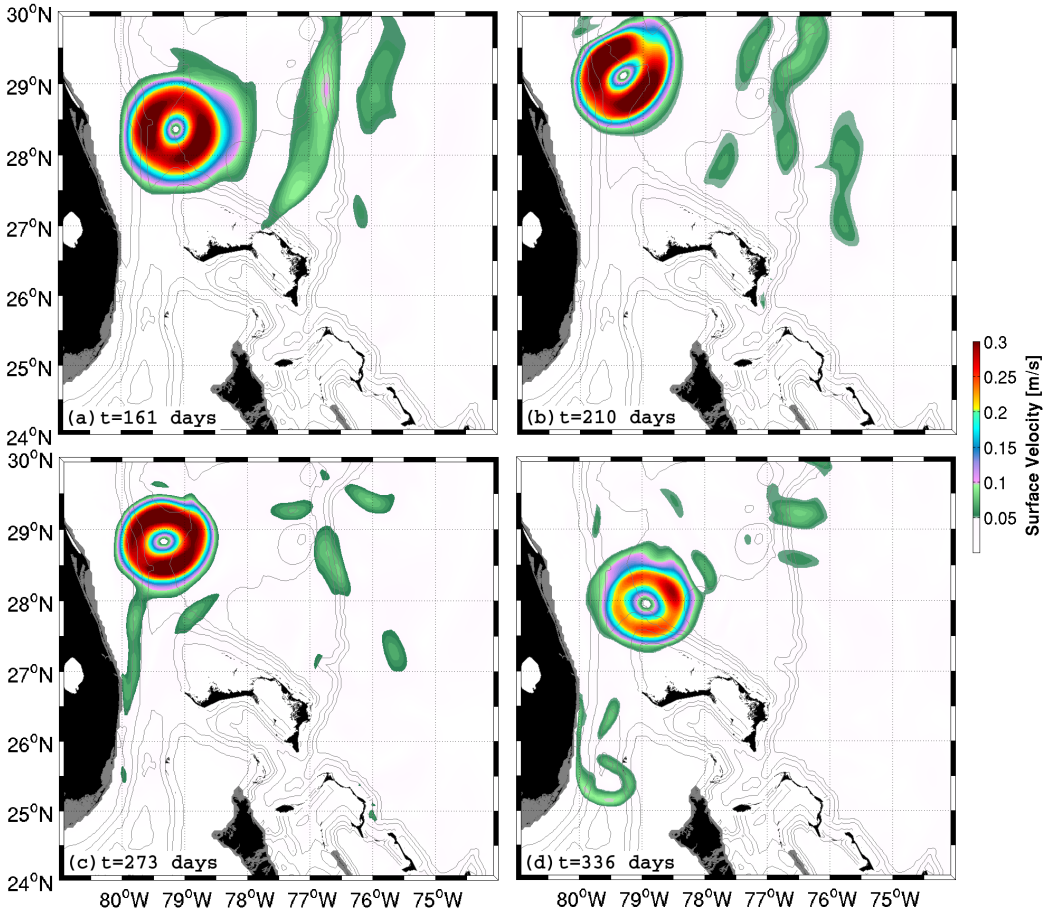

Figure 26: Surface velocity in the proximity and at the Florida Straits for experiment Prel-E03 at: (a) day 161, (b) day 210, (c) day 273, and (d) day 336.